Chapter 4

Efficient High-Performance Modified Slotted Patch Antennas using Metasurface for Dual-band Applications

4.1 Introduction

The last chapter discusses a portable, directive, and efficient metasurface-based fractal patch antenna in which an array of square-shaped patches are designed on top of the patch. Fractal geometrics, in combination with a dielectric via, have been integrated into the patch to shift the frequency of operation in the desired frequency region. This prototype employed the defective ground concept by incorporating two rectangular slots in the ground plane. The limitation of that antenna is that it offers a narrow bandwidth and the patterns in the E-plane and H-plane are deviated toward -34^0 and are asymmetric due to the feed offset and the leakage of out of phase fields from few slots either in the ground plane or at the patch.

This chapter addresses the design and analysis of multi-layered dielectric metasurface antennas (MSAs) for wideband applications. Two distinct source antennas have been employed for the MSA designs. These structures are simple to implement and control in new applications that make use of a planar antenna. Further, these antenna designs can be easily integrated and controllable with a planar antenna for new applications. The influence of MSA is more owing to the multi-functional behaviour viz., low profile, flexible, inexpensive, ease of integration and fabrication, isolation enhancement, backfire to endfire beam scanning capabilities, dual or wideband, and high gain with directive radiation characteristics [96-109]. The design and development of dual-band antennas have presented numerous challenges to the advancement of modern communication systems, as well as the introduction of various operating frequency ranges and numerous wireless standards [104], [114-115]. The dual-band antennas can deliver a strong and consistent wireless connection even in remote locations [104], [114]-[115]. A dual-band antenna can send and receive radio frequency signals at two distinct frequencies. These antennas can use either of the two frequencies separately or simultaneously, depending on their configuration. Dual-band antennas can give ultimate performance and flexibility. Some of the devices can connect to one frequency while the others can connect to the second frequency to achieve better speed and range [104], [114]-[115]. In certain instances of antenna design, space control is a critical parameter in addition to the cost reduction [104], [114]-[115].

The first antenna design uses a metasurface (MS) based high-performance antenna with split ring resonators (SRRs) placed in the radiating patch's square slots. In this chapter, a portable, dual, wideband, directive, and high gain MS-based corner cut rectangular patch antenna has been proposed in which the MS and the radiating patch lie in the same plane. The defected ground has been realized in the ground surface by incorporating an array of rectangular slots. This results in the reduction of surface waves that minimizes the cross-polarized radiation [68, 151]. The antenna performance has been enhanced by introducing a 4×5 order MS on the upper region and two 1×4 array of unit cells just adjacent to the conventional patch. The equivalent circuit model of SRR [152], as well as the proposed unit cell, have been addressed in detail in this chapter. The prototype has been analyzed using Ansys HFSS [126] and it provides a satisfactory return loss of 42 dB at 11.65 GHz. Furthermore, the designed prototype carries dual frequency bands ranging from 9.03 GHz to 9.60 GHz and 11.23 GHz to 14.52 GHz with the respective fractional bandwidths of 4.02% and 28.24%. After the incorporation of the MS design, the gain of 10.66 dBi with unidirectional radiation characteristics has been accomplished at 14.44 GHz. The proposed prototype has been fabricated and the experimental measurements have been carried out in the anechoic chamber. It is found that the measured results are in good agreement with the simulated ones. In the second antenna design, the prototype is highly efficient, directive, and dual-band which finds applications in C-band and X-band. A 7×7 order MS structure has been placed as a superstrate configuration just above the radiating element separated by an air spacer. The prototype has been analyzed using Ansys HFSS [126] and it offers satisfactory impedance bandwidths at C- and X- bands. The detailed circuit model analysis has been sequentially developed to validate the impedance behavior of the proposed antenna configuration. The MS antenna exhibits the fractional bandwidths of 6.1% and 35.15% centered at 4.26 GHz and 8.62 GHz respectively while the maximum realized gain of 8.72 dBi has been achieved at 10.99 GHz with endfire radiation characteristics along the boresight direction. The proposed prototype has been fabricated and the experimentally measured results offer good agreement with the simulated ones.

4.2 Design Analysis of the Single-Layered Metasurface Antenna

4.2.1 Geometry of Antenna

The proposed structure consists of a split ring resonator (SRR) based corner cut rectangular patch antenna with MS printed on a 30×47 mm^2 FR4 substrate of the thickness of 1.6 mm, having a dielectric constant of 4.4 and loss tangent of 0.025. The 4×5 order MS is placed on the upper region of the patch whereas two 1×4 arrays of unit cells are arranged adjacent to the patch surface. The defected ground has been realized by using five symmetric rectangular slots of dimension 1×2 mm^2. The SRR based corner cut rectangular patch antenna and the MS are placed together in the same plane. So it makes the proposed antenna compact and low-profile. The overall structure of the proposed prototype is described in Fig. 4.1(a).

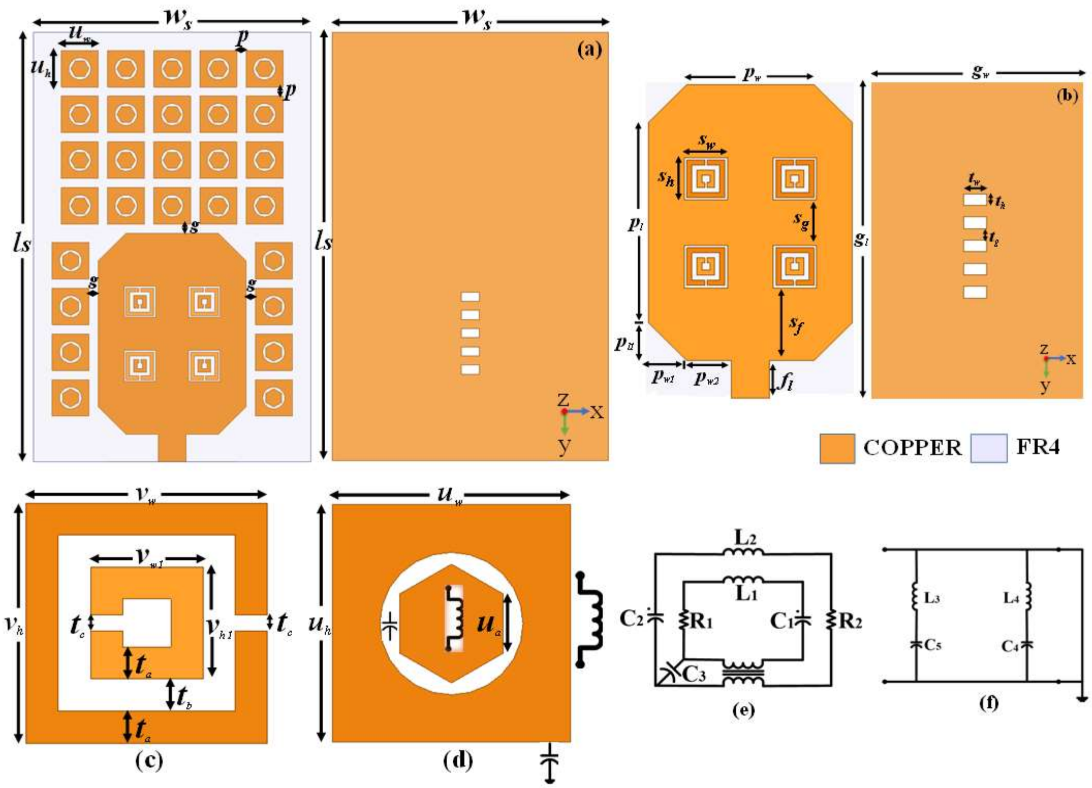

Fig. 4.1. (a) Proposed structure with top and bottom surfaces (b) Conventional patch with top and bottom surfaces (c) SRR (d) Proposed unit cell (e) Equivalent circuit model of SRR (f) Equivalent circuit model of the proposed unit cell. R_1, R_2, L_1, L_2, L_3, L_4, C_1, C_2, C_3, C_4, and C_5 are the resistances, inductances, and capacitances of the SRR and the proposed unit cell.

The detailed dimensions of the unit cell of the MS structure are described in Fig. 4.1(d). The equivalent circuit model of SRR and the proposed unit cells are illustrated in Fig. 4.1(e) and

Fig. 4.1(f) respectively. Consequently, the equivalent circuit model for the proposed prototype has been mentioned in Fig. 4.2.

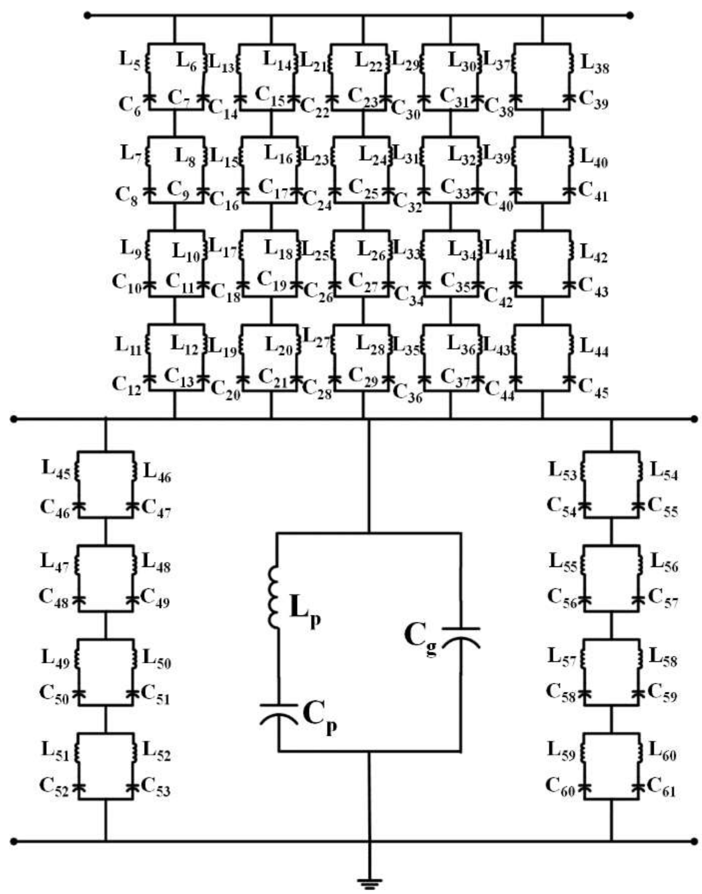

Fig. 4.2. Equivalent circuit model of the proposed MS structure. Numbered in sequence from 5, 6, 7…, 58, 59, and 60 for the subscript of inductance (L) and numbered in sequence from 6, 7, 8…, 59, 60, and 61 for the subscript of capacitance (C) are the total number of inductances and capacitances mentioned different unit cells. L_p and C_p are the equivalent inductance and capacitance of the conventional patch in which C_g is the ground capacitance. Here, the resistances are neglected.

The equivalent circuit model of Fig. 4.1 has been designed in Fig. 4.2 for the analysis and study. In this design, the circuit model is not verified, here only the model has been mentioned. This is a schematic according to the arrangement of unit cells and the patch. In the same chapter, a multi-layered MSA has been discussed briefly. Here the circuit model simulation is verified with full-wave simulation.

Table 4.1. The optimized geometrical parameters of the proposed antenna

Optimized Parameters	Dimension (mm)	Optimized Parameters	Dimension (mm)	Optimized Parameters	Dimension (mm)
w_s	30	P_{w1}	3	t_w	2
l_s	47	P_{w2}	3.5	t_g	1
u_w	4	$s_w=s_h$	3.4	t_h	1
u_h	4	S_f	5.8	$v_w=v_h$	3
$p=g$	1	S_g	3.6	$v_{w1}=v_{h1}$	1.4
p_w	10	f_1	3	$t_a=t_b$	0.4
p_l	16	g_w	16	t_c	0.2
P_{l1}	3	g_l	22	u_a	1

The values of the inductance L_m and the capacitor C_m of the MS can be approximately calculated from 4.1-4.2 [102]

$$L_m = \mu h \tag{4.1}$$

$$C_m = \frac{u_w \varepsilon_0 (1+\varepsilon_r)}{\pi} \cosh^{-1}\left(\frac{2u_w+p}{p}\right) \tag{4.2}$$

Here, h is the height of the substrate, u_w is the width of the unit cell patch and *p* is the gap between two consecutive unit cells. The bandwidth of the MS in-phase reflection can be expressed as (4.3)

$$BW = \frac{1}{\eta}\sqrt{\frac{L_m}{C_m}} \tag{4.3}$$

The values of L_{eq} and C_{eq} can be calculated by the effect of the L_p along with L_m and C_m along with C_p and C_g. The resonant frequency (f_0) of the antenna is obtained by using the equivalent circuit analysis method and mentioned in (4.4), where L_{eq} and C_{eq} are effective inductance and capacitance of the antenna

$$f_0 = \frac{1}{2\pi\sqrt{L_{eq}C_{eq}}} \tag{4.4}$$

The detailed dimensions of the complete structure are provided in Table 4.1. Parametric studies are performed to explore the design parameters of the antenna. Initially, a profile closer to half wavelength has been selected based on the operating frequency. The patch dimensions Pw and Pl are tuned for required resonant frequencies. Next, the positions of the slots in the ground plane along with the slot length dimension can be changed to tune the frequencies. Here, the slots are always placed symmetrically along the feed direction. The individual arm lengths are smaller than quarter-wavelength at the radiating frequencies. The antenna is excited by a 50Ω microstrip feedline applied with respect to the ground plane.

4.2.2. Design of the Patch Antenna

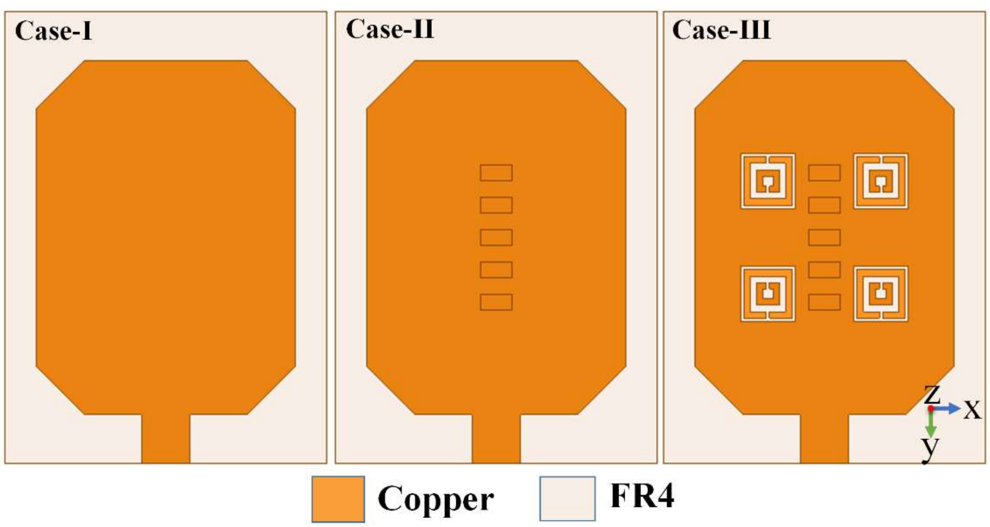

Fig. 4.3. Design steps of conventional patch antenna with different modifications.

The design evolutions of the conventional patch antenna with different modifications have been illustrated in Fig. 4.3 and their respective reflection coefficient responses are provided in Fig. 4.4. Initially, the corner cut rectangular patch is designed without any defects or slots which is shown in Case-I of Fig. 4.3. Here, the antenna operates at dual frequencies viz., 12.78 GHz and 14.05 GHz offering fractional bandwidths of 2.2% and 2.4% respectively. In addition, the maximum realized gain of 3.65 dBi has been achieved at 14.05 GHz. Later, the defective ground has been formed by introducing five rectangular slots of size 1×2 mm^2 which is depicted as Case-II of Fig. 4.3. The gap between the two consecutive rectangular slots is 1 mm.

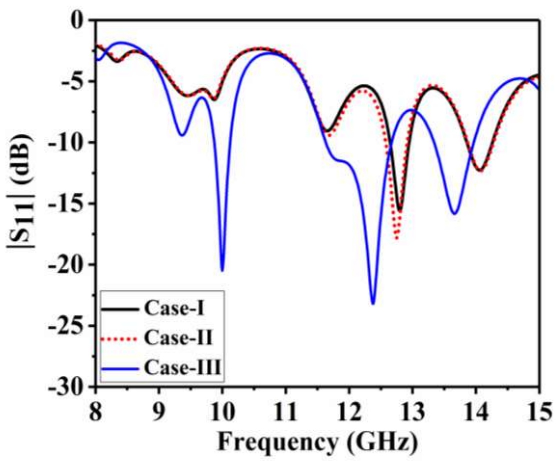

Fig. 4.4. The plot of $|S_{11}|$ (dB) with respect to frequency (GHz) for different antenna modifications.

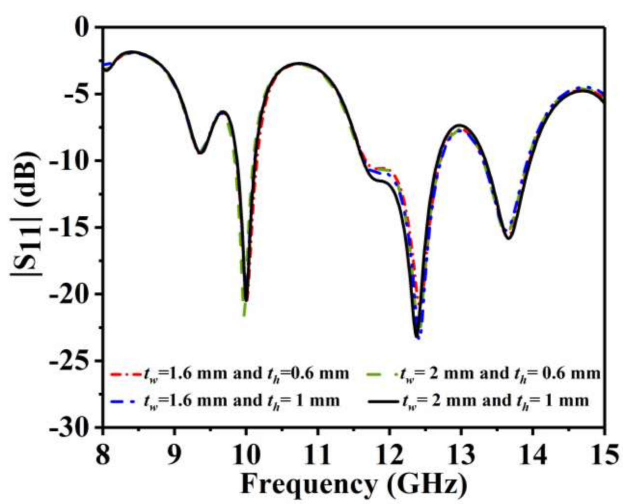

Fig. 4.5. The plot of $|S_{11}|$ (dB) with respect to frequency (GHz) for rectangular slots width (t_w) and length (t_h) variation.

The parametric variation of the ground slot width (t_w) and length (t_h) has been mentioned in Fig. 4.5. It has been observed that at t_w = 2 mm and t_h = 1 mm the ground plane reflection characteristics remain invariant with respect to frequency. Here, the fractional bandwidths have been enhanced to 2.5% and 2.9% at 12.76 GHz and 14.08 GHz respectively; but, the realized gain has been reduced to 3.21 dBi.

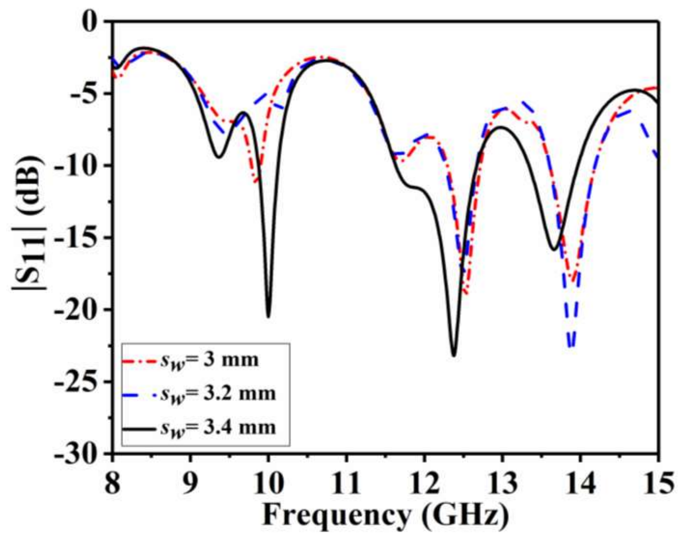

Fig. 4.6. The plot of $|S_{11}|$ (dB) with respect to frequency (GHz) at (s_w) variation.

The incorporation of the larger number of rectangular slots in the ground surface leads to the improvement of the antenna performance with degraded radiation patterns. Hence, the number of rectangular slots in the ground plane has been limited to five so that the improvement of radiation patterns of the antenna can be realized by maintaining better performance. Further, four 3×3 mm^2 SRRs are embedded into four 4×4 mm^2 square slots (s_w) on the patch which is illustrated in Case-III of Fig. 4.3. The parametric variation of the slot width (s_w) with respect to frequency has been shown in Fig. 4.6. When the slot width is increased, the frequency of operation shifts to a lower frequency region, and the impedance bandwidth improves.

The SRR structure in the prototype behaves like a simple RLC resonator with a few constructive and destructive couplings [152, 153]. Hence, the SRRs have been incorporated into the patch to minimize the ohmic loss. As a consequence, it improves the gain of the antenna. The antenna with the incorporation of SRR-embedded square slots operates at three distinct operating frequencies viz., 10 GHz, 12.38 GHz and 13.67 GHz with fractional bandwidths of 2.5%, 8.3% and 4.4% respectively. In addition, the realized gain has been enhanced to 6.1 dBi at 12.38 GHz. Therefore, the antenna mentioned in Case-III of Fig. 4.3 has been considered as the conventional patch antenna due to its improved performance. Further, the performance of the antenna can be further enhanced by incorporating an MS layer with the radiating patch.

4.2.3. Geometry of Metasurface Unit cell

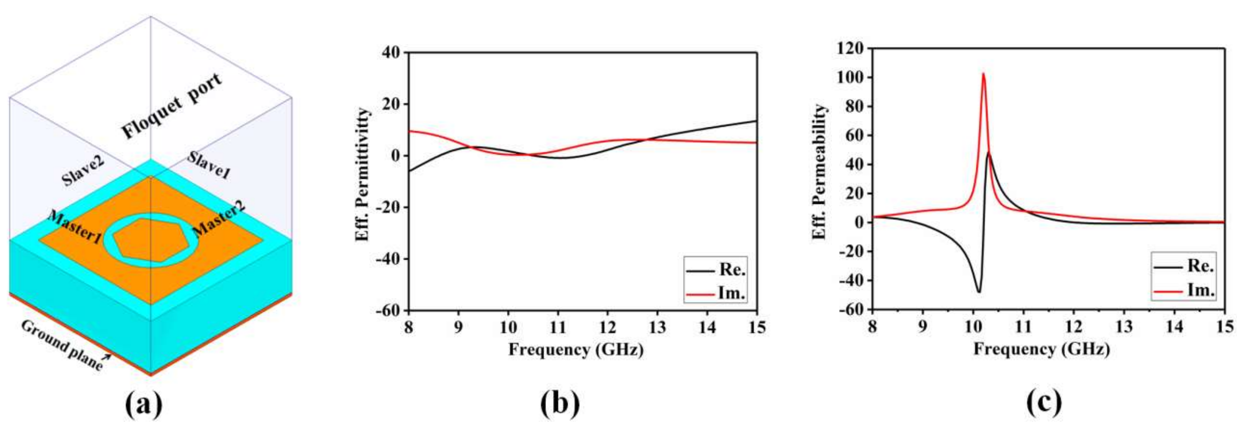

Fig. 4.7. (a) The 3D view (b) Effective permittivity and (c) Effective permeability of the unit cell.

The overall size of the unit cell is 4×4 mm^2. The unit cell consists of a square patch of dimension 4 mm in which a circular slot of 1.2 mm radius has been etched out. Further, in the circular slot, a concentric hexagonal patch having each side of dimension 1 mm has been designed. Here the MS is formed by 4×5 order unit cells placed on the upper region of the conventional patch together with two 1×4 array of unit cells arranged adjacent to the conventional patch. The two-unit cells are arranged in such a way that it follows the homogeneity properties of MS [15-17].

The 3D view of the unit cell is mentioned in Fig. 4.7(a) and it is excited incorporating periodic boundary conditions using Ansys HFSS. Port represents the surface through which a signal enters or exits the geometry. Coupled Master and slave boundaries are used to model a unit cell of a repeating structure. Master and slave boundaries are always paired. The master and slave surfaces must be of identical shapes and sizes and illuminated by Floquet ports so that the periodic boundary conditions with various Floquet modes are excited. A coordinate system must be identified on the master and slave boundary to identify point-to-point correspondence. These are useful in creating unit cells and arrays. The electromagnetic properties, such as the complex permeability (μ) and the permittivity (ε) can be evaluated either by the analytical Drude-Lorentz model or by the S-parameter retrieval method [47-49]. In this case, the S-parameter extraction method has been employed. The comparable relative permittivity ε_r and permeability μ_r may be calculated using the values of S_{11} and S_{21}. First, using (1.11) and (1.12) from [47-49], the equivalent impedance Z and the reflective index n of the MS are always determined. The basic electromagnetic behaviors of effective permittivity and permeability of the MS layer have been studied and analyzed. The real and imaginary parts of the same are illustrated in Fig. 4.7(b) and Fig. 4.7(c) respectively. The MS layer behaves as a left-handed material (LHM) in the frequency band 10-12 GHz. LHM materials are convenient for wideband, directive and high gain antenna applications [83-94]. The unit cells of the MS are arranged in such a way that, they can diffuse the unwanted reflection uniformly and avoid the reflection in the specular direction. The parametric study of the gap between the two consecutive unit cells (p) of MS and the gap variation between the unit cell and the radiating patch (g) are shown in Fig. 4.8. From Fig. 4.8(a) and Fig. 4.8(b), it can be clearly observed that at p = 5 mm and g = 1 mm, the antenna offers maximum return loss with enhanced bandwidth. Fig. 4.9 demonstrates the effect of the unit cell width (u_w) in terms of impedance bandwidth and return loss. It has been observed that when the width (u_w) of the unit cell is optimized to 4 mm, the impedance bandwidth is high with improved return loss characteristics.

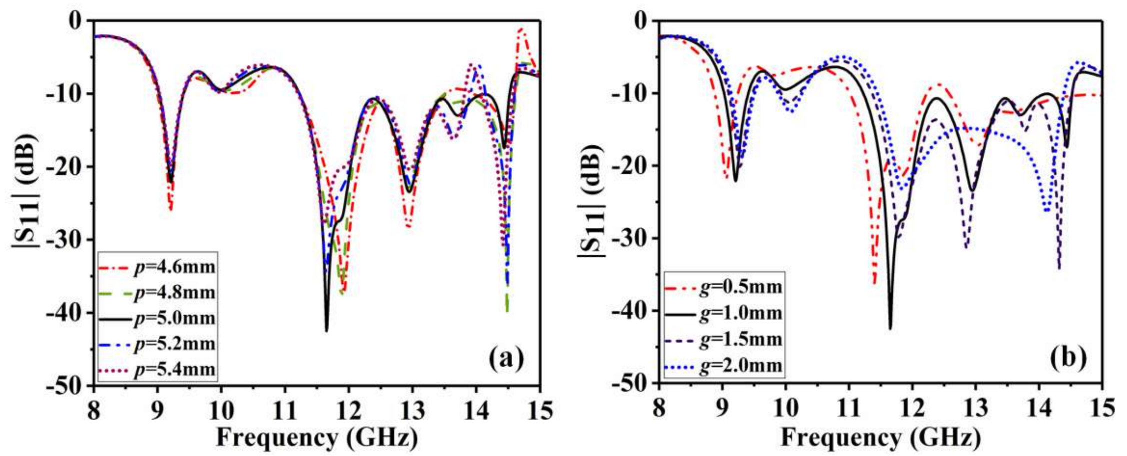

Fig. 4.8. Plot of $|S_{11}|$ (dB) with respect to frequency (GHz) (a) at different p-variations and (b) at different *g-variations*.

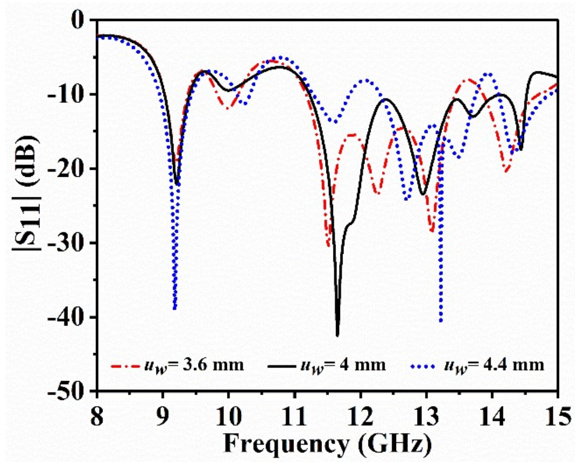

Fig. 4.9. Plot of $|S_{11}|$ (dB) with respect to frequency (GHz) at different u_w-variations.

Further, at p = 5 mm, it follows the homogeneity properties of MS [15-17]. Initially, the conventional antenna provides narrow bands with low gain but after placing the MS together with the conventional patch, the resonance frequency of the antenna has detuned due to the mutual coupling between the two. Therefore, the gap between two adjacent elements have been systematically optimized for achieving the dual-band operation at the desired resonant frequency with improved reflection coefficient.

4.3. Results and Discussion of the Single-Layered Metasurface Antenna

4.3.1. Simulated Results

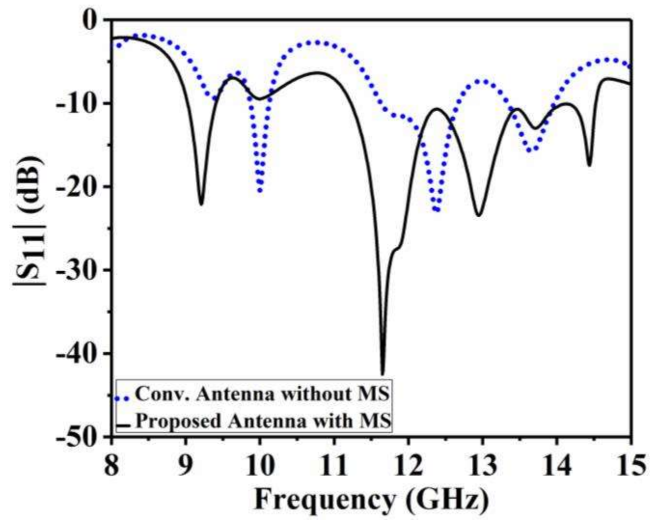

Fig. 4.10. The plot of $|S_{11}|$ (dB) with respect to frequency (GHz) for different antenna variations.

The analysis and optimization of the overall structure have been performed by full-wave simulation software Ansys HFSS [126]. The return loss responses with and without incorporation of the MS layer are provided in Fig. 4.10. As observed in Fig. 4.10, the conventional antenna effectively operates in three frequency bands viz., 10 GHz, 12.38 GHz, and 13.67 GHz with impedance bandwidths of 2.5%, 8.31%, and 4.4% respectively. As the reference antenna exhibits a narrow band response, so the return loss characteristics of the conventional antenna have been further improved by incorporating the MS layer in the same plane of FR4 dielectric.

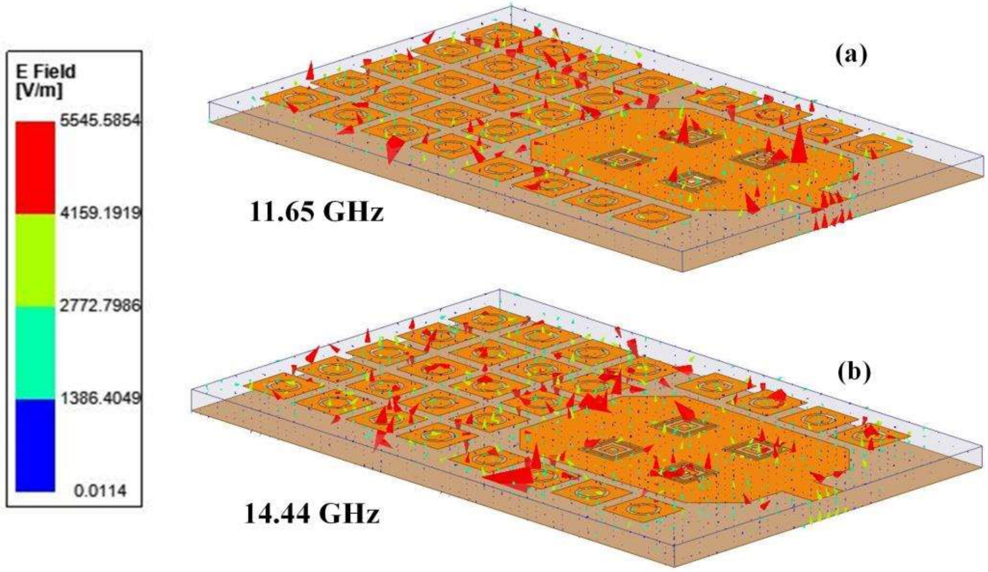

Fig. 4.11. Electric field distributions of the proposed prototype at (a) 11.65 GHz and (b) 14.44 GHz.

In this case, the frequency bands have been shifted to the lower frequency side, as compared to the conventional patch antenna. The wide impedance bandwidth over the frequency band 9.03 GHz to 9.60 GHz and 11.23 GHz to 14.52 GHz has been achieved by incorporating the MS layer in the patch. Further, the antenna integrated with MS shows excellent impedance matching with $|S_{11}|$ less than −21 dB at 9.20 GHz and less than -42 dB at 11.65 GHz. The same antenna with an embedded MS layer yields a good reflection coefficient at both the frequency bands and the impedance bandwidths of 4.02% and 28.24% have been achieved.

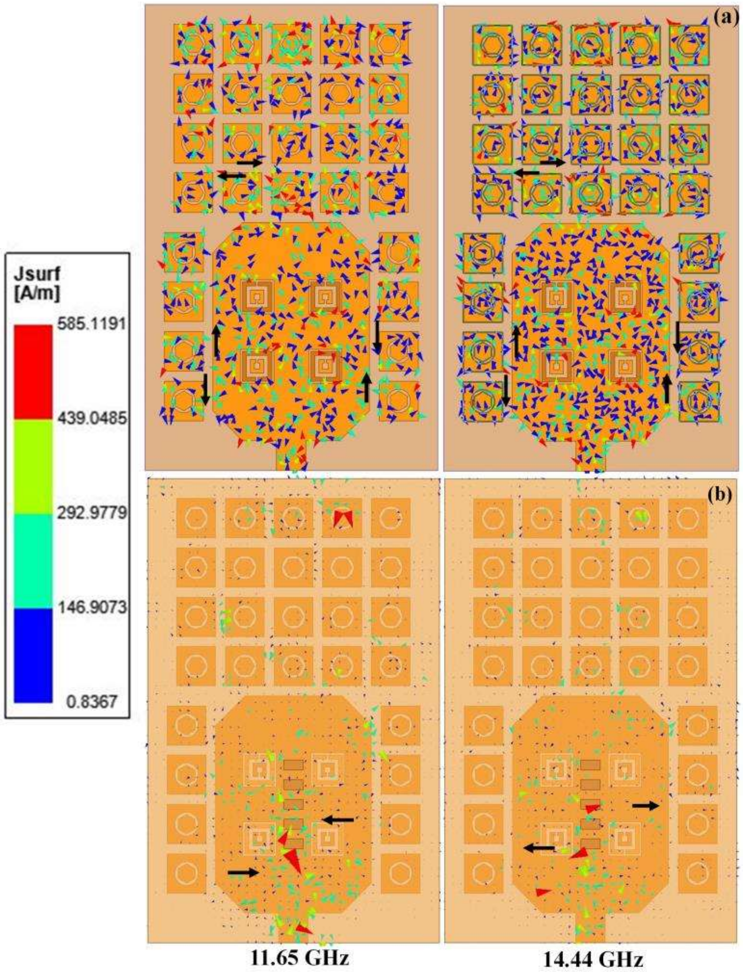

Fig. 4.12. Surface current distributions of the proposed prototype at (a) top and (b) bottom surfaces.

The electric field distributions and surface current distributions of the MS loaded antenna with top and bottom surfaces at 11.65 GHz and 14.44 GHz have been shown in Fig. 4.11 and Fig. 4.12 respectively. The electric field are densely concentrated on the MS layer and the slot position of the patch at 14.44 GHz. The MS layer plays a significant role in reflecting the electric field as observed around the antenna location. The surface current are intense around the antenna aperture due to slots in the radiating patch and the ground surface. The coupling currents between the patch slots and the MS unit cells are lower at 14.44 GHz.

4.3.2. Measured Results

The antenna prototype has been printed on FR4 dielectric by employing an LPKF PCB Prototyping Instrument [130]. The top and bottom views of the printed antenna are given in Fig. 4.13(a) and Fig. 4.13(b) respectively. The antenna prototype has been tested using Keysight Vector Network Analyzer with model N9951A by adopting some standard calibration techniques as shown in Fig. 4.13(c) [154].

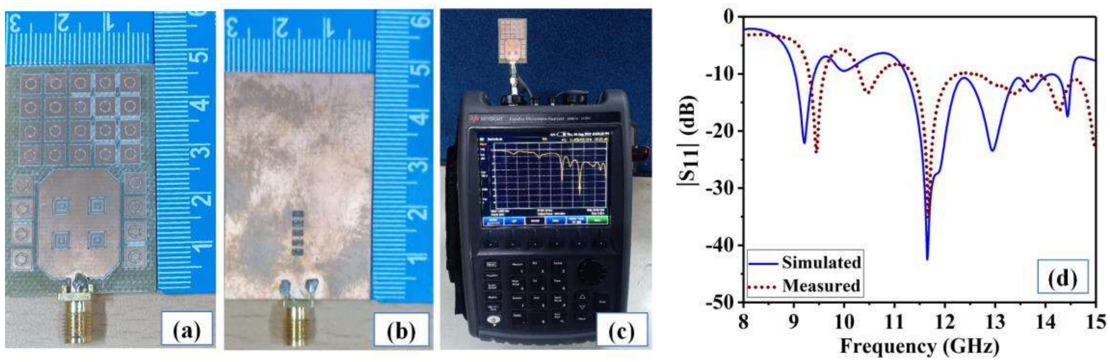

Fig. 4.13. Proposed fabricated structure (a) top view (b) bottom view (c) S-parameter measurement of using VNA (d) Plot of Simulated vs Measured $|S_{11}|$ (dB) with respect to frequency.

All the experimental measurements are performed within the anechoic chamber. The measured return loss profile of the proposed antenna is presented in Fig. 4.13(d) where it is compared with the simulated one. It is found that experimentally measured 10 dB impedance bandwidth has been achieved in the dual-frequency regions ranging from 9.29 GHz-9.60 GHz and 11.30 GHz-15 GHz. Moreover, the maximum return loss of 35 dB has been achieved at 11.67 GHz; resulting in good matching with the simulated response. Some discrepancies have been noticed between the simulated and measured responses in the range 11-15 GHz which may be attributed due to the dispersive nature of the FR4 substrate.

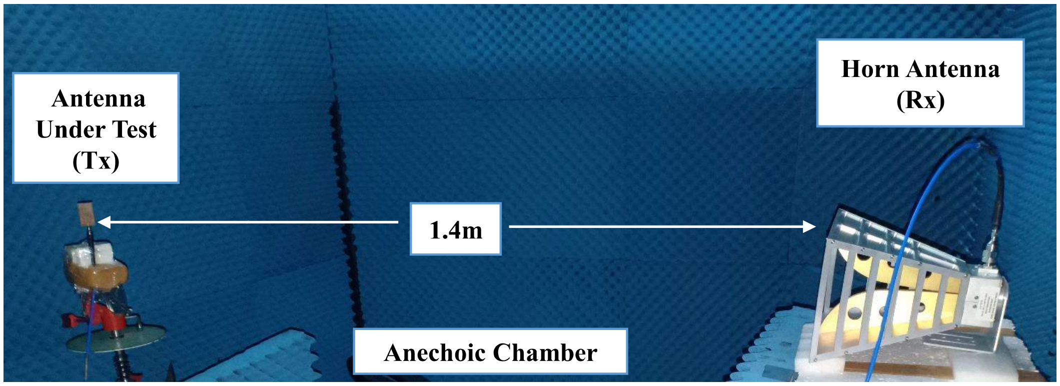

Fig. 4.14. Far-field measurement using an anechoic chamber.

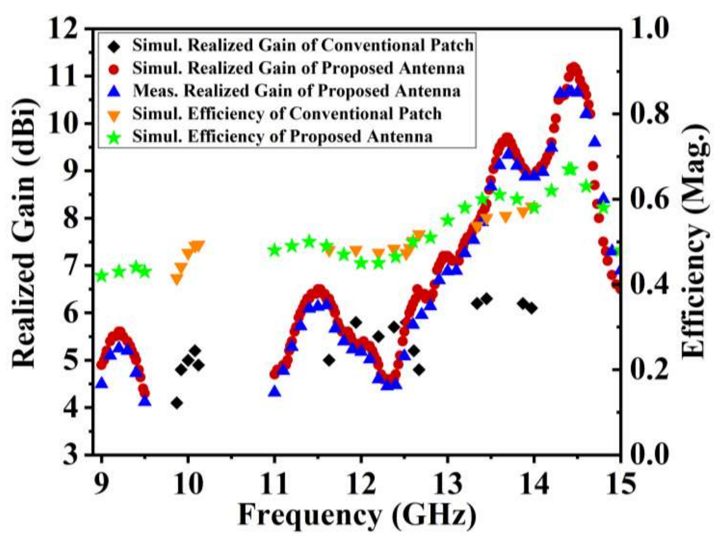

Fig. 4.15. Responses of Realized Gain (dBi) and Efficiency (Mag.) at different operating frequencies within the conventional patch and the proposed antenna.

The E-plane and H-plane radiation pattern measurements of the fabricated antenna have been performed by a fixed-mount ridged type Vivaldi-based horn antenna operating in the frequencies from 1-18 GHz [155]. The standard horn (Rx) and positioning system for the antenna under test (Tx) are separated by 1.4 m. The Tx and Rx antennas are kept in the far-field region as shown in Fig. 4.14 by making a separation of 1.4 m among them. The performance responses of the realized gain (dBi) and efficiency of the conventional patch and the proposed MS antenna at different operating frequencies are illustrated in Fig. 4.15.

As revealed from the plots, the maximum realized gain of 10.66 dBi has been achieved at 14.44 GHz which is nearly 4.5 dBi higher than the conventional antenna. The simulated and measured realized gains are in good agreement. The gain of the antenna has been enhanced to a significant level after the incorporation of 4×5 order MS at the upper surface and two 1×4 array of unit cells placed adjacent to the radiating patch. Besides, it has been further observed from Fig. 4.15 that the maximum radiation efficiency of the proposed antenna is 67% at 14.44 GHz.

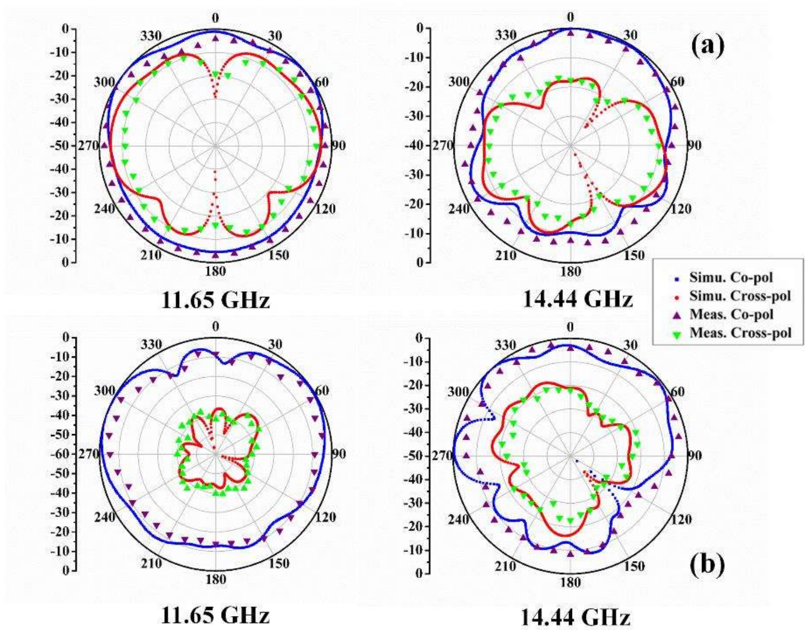

Fig. 4.16. Co-polarized and Cross-polarized (a) E-plane and (b) H-plane at different operating frequencies within the proposed structure.

The simulated and measured E-plane ($\varphi = 0^0$) and H-plane ($\varphi = 90^0$) radiation pattern characteristics of the proposed antenna have been depicted in Fig. 4.16(a) and Fig. 4.16(b) respectively at the operating frequencies of 11.65 GHz and 14.44 GHz. Unidirectional radiation pattern has been observed both in E-plane and H-plane at the operating frequencies as evident from the co-polarized radiation patterns. It is further observed that the cross-polarization levels are at least 20 dB below that of the co-polarization levels both in E and H-planes. In the far-field measurement, the cross-polarization levels are suppressed at different frequencies due to the incorporation of the metasurface placed just above the patch. A little discrepancies arising among the measured and simulated results of the frequency band and far-field radiation characteristics may be due to fabrication tolerances, dielectric loss, and cable and adaptor losses.

Table 4.2. Comparison Table for the performance of the proposed antenna with existing GHz antennas.

Antenna Literature	**Overall Dimensions**	**Operating Frequency (GHz)**	**Design Complexity**	**Antenna Cost**	**Fractional Bandwidths (%)**	**Realized Gain (dBi)**	**Efficiency (%)**	**Antenna Type**
Pan *et al.* [141]	$1.3\lambda_0\times1.3\lambda_0\times0.6\lambda_0$	5	High	High	Wide (28.4)	8.2	39	Superstrate technology with MS
Cao *et al.* [142]	$1.16\lambda_0\times1.16\lambda_0\times0.26\lambda_0$	5.1	High	High	Medium (11.5)	9.3	-	AMC
Kim *et al.* [143]	$1.2\lambda_0\times1.2\lambda_0\times0.4\lambda_0$	5.75	Very High	High	Narrow (2.7)	6.8	-	Holey dielectric superstrate structure
Liu *et al.* [144]	$1.7\lambda_0\times1.7\lambda_0\times0.02\lambda_0$	10.6	High	Low	Narrow (7.9)	6.2	15.8	Perfect Absorber material as a substrate
Sharma *et al.* [145]	$3.6\lambda_0\times3.6\lambda_0\times0.14\lambda_0$	13.3	High	Low	Narrow (9.0)	9.1	-	Chess-board based polarization conversion metasurface
Zheng *et al.* [150]	$2.8\lambda_0\times2.8\lambda_0\times0.1\lambda_0$	10.5	Very High	High	Medium (18.5)	8.1	-	AMC
Alibakhshikenari *et al.* [156]	$2.4\lambda_0\times3.2\lambda_0\times0.04\lambda_0$	8	Low	Low	Medium (14.5)	7	88.7	Antenna arrays based on metamaterial EBG structure
Alibakhshikenari *et al.* [157]	$2.6\lambda_0\times1.1\lambda_0\times0.06\lambda_0$	11.65, 13.56, 15, 17.9 (Quad band)	Low	Low	Narrow (3.88, 8.62, 9.95), Wide (23.32)	8.2 (Maximum)	-	Antenna arrays using slot

Alibakhshikenari *et al.* [158]	$2.1\lambda_0\times1.4\lambda_0\times0.05\lambda_0$	9.8	Low	Low	Medium (17.28)	7.85	92.78	Antenna arrays with metamaterial photonic bandgap
Zheng *et al.* [159]	$2.2\lambda_0\times2.2\lambda_0\times0.6\lambda_0$	10.80	High	High	Medium (16.3)	12	-	Chessboard arranged metamaterial superstrate
Long *et al.* [160]	$1.24\lambda_0\times1.24\lambda_0\times0.65\lambda_0$	9.6	High	High	Narrow (8.8)	11.73	-	Polarization conversion metasurface and partially reflecting surface
Li *et al.* [161]	$1.87\lambda_0\times1.87\lambda_0\times0.38\lambda_0$	8.5	High	High	Medium (13.8)	11.2	-	Chessboard polarization conversion metasurface
Sabapathy *et al.* [162]	$2.1\lambda_0\times0.7\lambda_0\times0.03\lambda_0$	5.8	High	High	Narrow (3.66)	7.5	-	Patch type antenna arrays
Debogovic *et al.* [163]	$2.3\lambda_0\times2.3\lambda_0\times0.52\lambda_0$	2	High	High	Narrow (3)	-	-	Varactor diode-based phased array
Ding *et al.* [164]	$2.34\lambda_0\times1.37\lambda_0\times0.27\lambda_0$	5.8	High	High	Narrow (4.61)	7.2	90	Planar phased array with pattern reconfiguration
Ji *et al.* [165]	$3.1\lambda_0\times3.1\lambda_0\times0.55\lambda_0$	5.5	High	High	Narrow (4)	12	-	Aperature coupling phased array and reconfigurable PRS structure
Proposed design	$\mathbf{1.16\lambda_0\times1.82\lambda_0\times0.06\lambda_0}$	**9.2, 11.65 (Dual-band)**	**Low**	**Low**	**Narrow (4.02), Wide (28.24)**	**2.8, 10.6**	**67**	**Metasurface based slotted patch**

The comparison of the proposed prototype with previously reported antennas is shown in Table 4.2. According to this table, it can be observed that the proposed antenna has achieved superior gain with enhanced bandwidth. Some of the reported antennas offer superior gain [54, 55, 56, 60] and maximum efficiency [36, 41, 59]; however, they have been realized by incorporating large dimensions along with high dielectric and low loss materials. In addition, the thickness of the antenna profile in all the cases are also very high as compared to the proposed antenna and the cost of these antennas are high due to the usage of costly substrates.

4.4. Design of the Multi-layered Metasurface Antenna

In the last design, the MS antenna is single-layered, dual and it operates in the X-band region only. Here the performance of the antenna has been improved by the MS with the combination of two different unit cells. In the current design, the efficiency and the other antenna features have been improved using multi-layered configuration. Further, the design, circuit model analysis, and realization of a novel metasurface-based low-profile slotted patch antenna for dual-band applications in C and X-bands have also been discussed in this section.

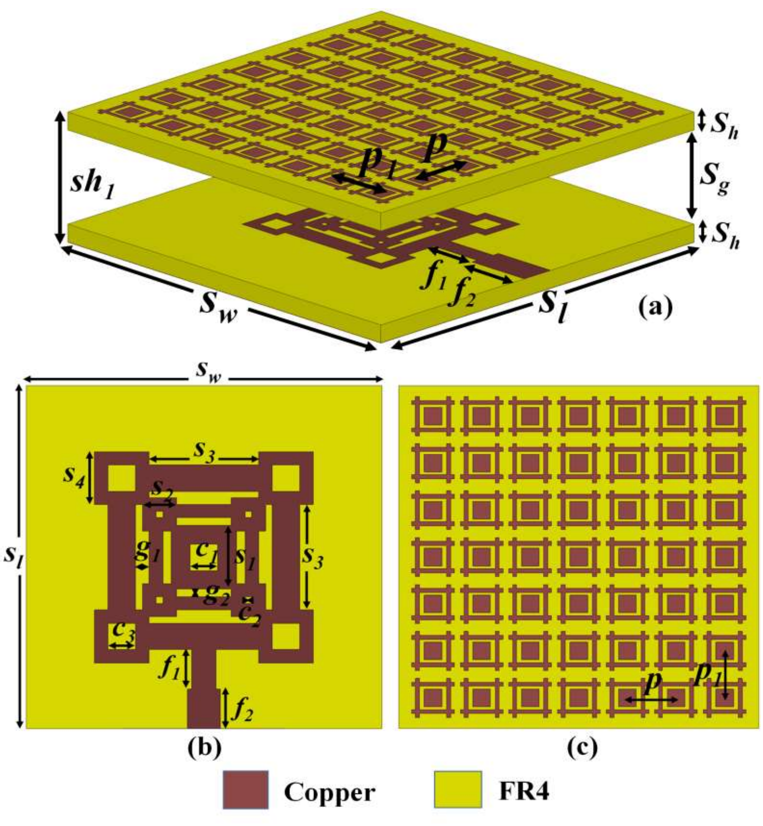

Fig. 4.17. (a) 3D geometry of the proposed structure, (b) conventional patch, (c) 7×7 order MS structure.

The antenna design comprises a modified slotted patch and a 7×7 array of periodic metasurface (MS) as superstrate configuration. The MSA comprises a slotted patch and a 7×7 order MS structure in which the patch is formed by square annular-shaped slots at the four corners. The MS layer is integrated with unit cells where each meta-atom composes of a centered patch surrounded by four rectangular strips. Both the radiating patch and the MS layer have been printed on a 1.6 mm thick FR4 dielectric layer (loss tangent = 0.025 and relative permittivity = 4.4) and separated from each other by the 2.2 mm thick air spacer. The three-dimensional (3D) geometry of the proposed structure with the conventional patch and 7×7 order MS superstrate layer have been represented in Figs. 4.17(a)-(c).

TABLE 4.3. The optimized geometrical parameters of the MS antenna

Optimized Parameters	Dimension (mm)	Optimized Parameters	Dimension (mm)
$S_w = S_l$	36	g_1	1
s_1	4.8	g_2	0.6
s_2	2.5	f_1	5
s_3	8	f_2	6
s_4	4	S_h	1.6
c_1	2	S_g	2.2
c_2	0.5	p	5.2
c_3	2	p_1	5

The detailed optimized dimensions of the proposed structure with the conventional patch and the MS have been provided in Table 4.3. The optimization and analysis of the proposed geometry have been performed using Ansys HFSS [166]. A brief discussion about the design evolution of the conventional patch antenna with their equivalent electrical circuit model have been shown in Figs. 4.18-4.22 respectively. The S_{11} response of the optimized design of each stage shown in Fig. 4.18 has been compared to the response achieved by the equivalent circuit model in Keysight Advanced Design System (ADS) [167]. Next, the design and analysis of the radiating patch with MS have been discussed. In this part, the circuit simulation of the proposed MS antenna has been discussed briefly and it is verified with the simulated result.

4.4.1. Design of the Conventional Patch

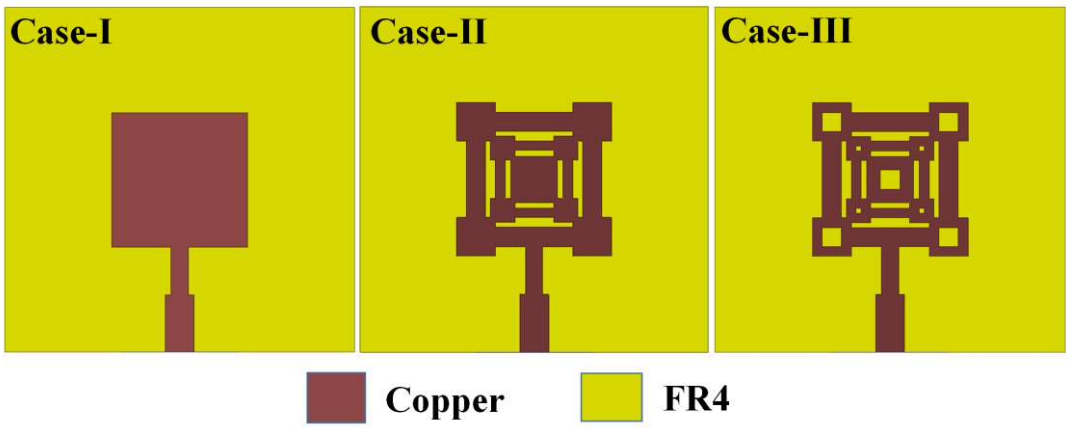

Fig. 4.18. Design steps of the conventional patch with different modifications.

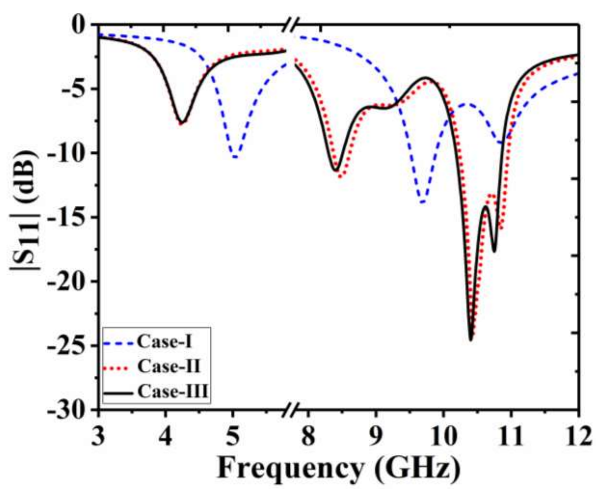

Fig. 4.19. The plot of $|S_{11}|$ (dB) with respect to frequency (GHz) for various modified antennas specified in Fig. 4.18.

Initially, a simple patch with a quarter-wave transformer feed has been used for impedance matching in order to minimize the energy when it is reflected from a patch antenna. The patch has been designed on a 1.6 mm thick FR4 substrate which is shown as Case-I in Fig. 4.18 First, the conventional edge-fed patch antenna has opted but the performance of the antenna has been degraded due to the improper impedance matching. The antenna with quarter-wave transformer feed operates at 5.04 GHz and 9.8 GHz with maximum impedance bandwidth of 3.7%.

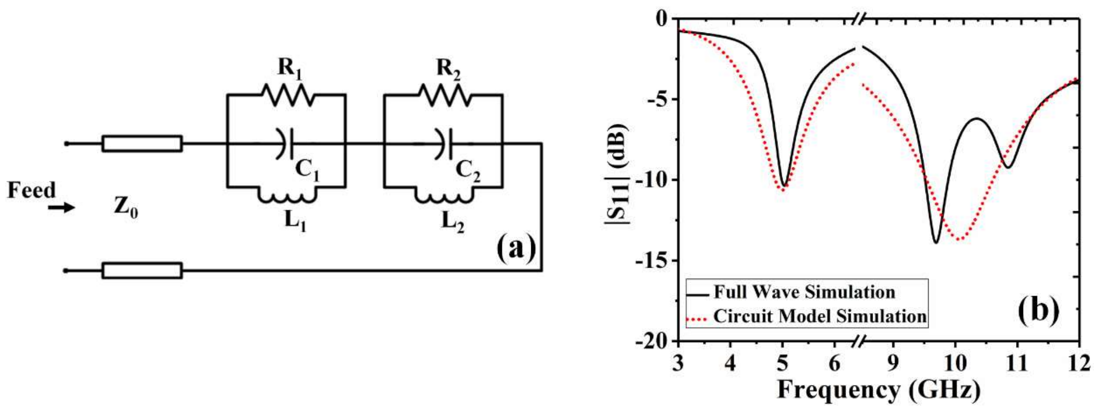

Fig. 4.20. (a) The equivalent electrical circuit model and (b) Ansys HFSS simulation vs ADS simulation characteristics of the simple patch antenna with quarter-wave transformer feed (Case-I).

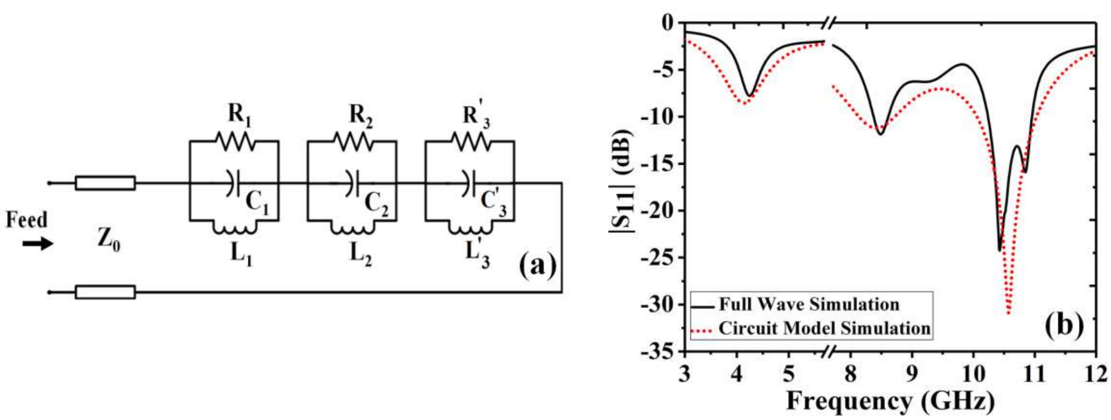

Fig. 4.21 (a) The equivalent electrical circuit model and (b) Ansys HFSS simulation vs ADS simulation characteristics of the slotted patch antenna with quarter-wave transformer feed (Case-II).

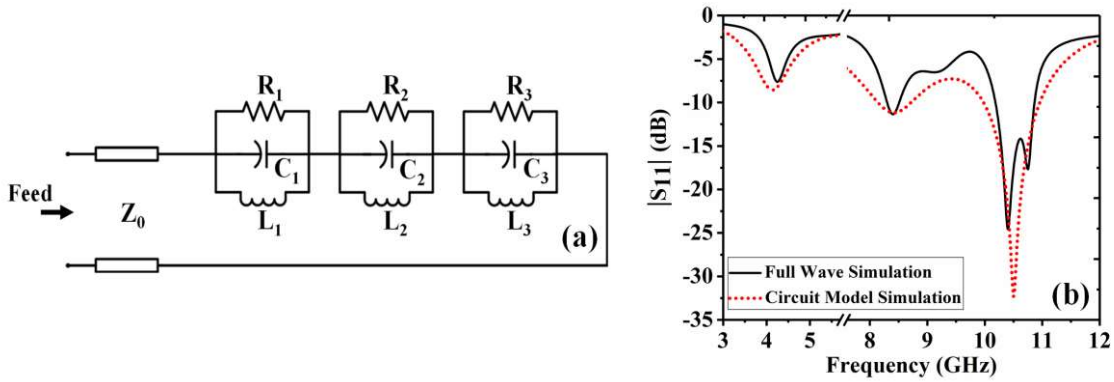

Fig. 4.22 (a) The equivalent electrical circuit model and (b) Ansys HFSS simulation vs ADS simulation characteristics of the conventional patch antenna with quarter-wave transformer feed (Case-III).

Next, in Case-II of Fig. 4.18, the microstrip patch has been reshaped into a slotted patch by inserting the square patches at the corners. This modified antenna operates again at dual frequencies with fractional bandwidths of 2.8% and 6.8% at 8.5 GHz and 10.46 GHz respectively. Further, the square patches have been reformed into square annular-shaped slots as illustrated in Case-III of Fig. 4.18. Therefore, the resonant frequencies of this antenna have been shifted towards the lower frequency regions due to the enhancement of the electrical length; thereby making the structure more compact in nature. The modified antenna operates at two distinct frequency regions ranging from 8.3 GHz to 8.51 GHz and 10.19 GHz to 10.87 GHz with minimum reflection co-efficient achieved at 8.42 GHz and 10.4 GHz respectively. The equivalent electrical circuit model of the antennas, shown in Fig. 4.18, has been subsequently developed using Keysight ADS [167]. The equivalent circuit components of the conventional antenna with different steps have been depicted in Figs. 4.20-4.22, where the radiating element is represented by the series connection of parallel RLC circuits [168]-[170].

The resultant input impedance of the equivalent circuit can be expressed in (4.5) [168]-[170]

$$Z_n = \sum_{k=1}^{n} \frac{j\omega R_k L_k}{R_k(1-\omega^2 C_k L_k)+j\omega L_k} \qquad (4.5)$$

Here, R_k represents the radiation resistance. L_k and C_k indicate the respective inductor and capacitor values corresponding to the slot resonator. The antenna elements are realized by the Foster canonical expression in which R_k takes care of both radiation and ohmic losses [168]-[170]. RLC parallel circuits in a series combination of the Foster canonical form is suitable to model the "electric antennas" which behave as an open circuit under DC excitation, whereas the magnetic antennas are represented by parallel connection of series RLC circuits and behave as short circuits under DC excitation [168]-[170].

The circuit representation for the simple patch antenna with quarter-wave transformer feed has been realized by incorporating two parallel combinations of RLC circuits in series [168]-[170]. The lumped parameters in Fig. 4.20(a) have been determined from the circuit model simulation studies as R_1 = 39.6 Ω, R_2 = 74.46 Ω, L_1 = 0.48 nH, L_2 = 0.35 nH, C_1 = 3.38 pF, C_2 = 1.11 pF and Z_0 = 50 Ω. Further, the reflection characteristics of the simple patch using Keysight ADS have been studied and compared with the simulated result from Ansys HFSS as shown in Fig. 4.20(b) and found to be in good agreement. Next, the circuit model of the antenna in Case-II of Fig. 4.18 has been realized by introducing an additional RLC circuit with the previous model (Fig. 4.20(a)). The passive elements R_1' = 95.2 Ω, L_1' = 0.18 nH and C_1' = 1.29 pF have been extracted from the circuit model simulation as represented in Fig. 4.21(a). In Fig. 4.21(b), the reflection characteristics of the modified patch have also been compared with the ADS simulation and it is observed that there is a little discrepancy in the first band. Later, the reflection characteristics have been improved by increasing the capacitance value due to the presence of the parasitic element in the form of slots in the third RLC combination as depicted in Fig. 4.22(a). It is observed from Fig. 4.22(b) that there is a minor frequency shift due to the increase of the capacitance value (Case-II of Fig. 4.18) into the slotted annular patch (Case-III of Fig. 4.18). Again, the same process has been followed to determine the lumped parameters as $R_3 = 94.5\ \Omega$, $L_3 = 0.18$ nH, and $C_3 = 1.31$ pF.

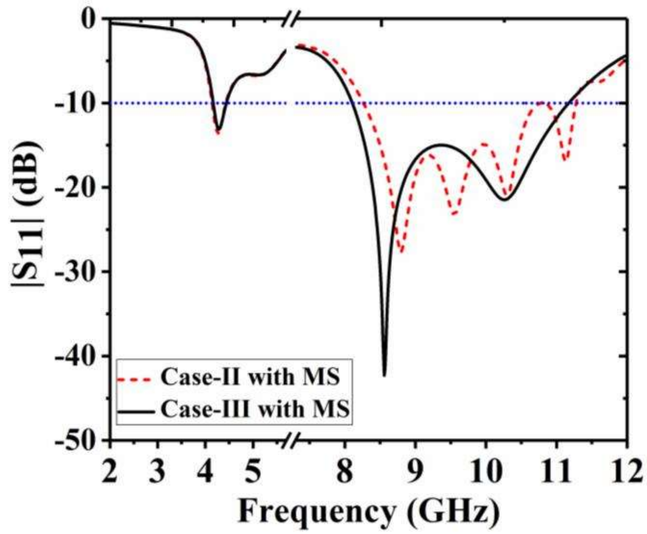

Fig. 4.23. Plot of $|S_{11}|$ (dB) with respect to frequency for Case-II and Case-III in Fig. 4.18 with MS.

The design and analysis of Case-II in Fig. 4.18 are simpler compared to Case-III in Fig. 4.18 from the above analysis however there is a significant improvement in the impedance matching and realized gain when the proposed MS structure is combined with the antenna designed in Case- III as compared to Case-II. It is observed from Fig. 4.23 that the antenna in Case-II with MS operates at three distinct frequencies ranging from 4.14 GHz to 4.42 GHz, 8.27 GHz to 10.76 GHz, and 10.84 GHz to 11.27 GHz whereas in Case-III, the antenna functions at two distinct frequencies, ranging from 4.18 GHz to 4.44 GHz and 8.11 GHz to 11.14 GHz. Additionally, the maximum realized gain of 6.4 dBi has been achieved in Case-II with MS, whereas it is 8.27 dBi in Case-III. The antenna shown as Case-III in Fig. 4.18 has been considered as the conventional patch for the rest of the study due to its superior performance as compared to the earlier ones (Case-I and Case-II).

4.4.2. Design of the Metasurface Antenna

The design of the MS layer has been formed with a periodical arrangement of 7×7 order unit cells. The MS layer has been placed above the conventional patch and separated by an air spacer of a thickness of 2.2 mm. The unit cell of the MS has been designed according to the operating wavelength and comprises a center patch surrounded by four rectangular strips of identical dimensions. The top view of the unit cell with geometrical dimensions has been shown in Fig. 4.24.

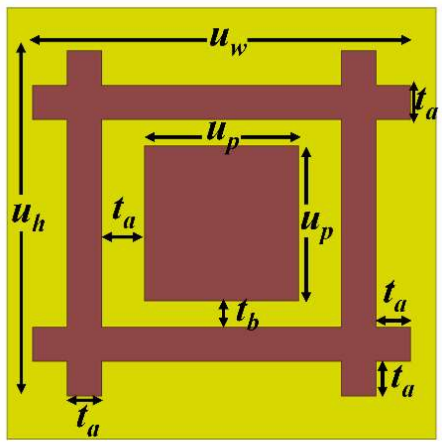

Fig. 4.24. The proposed unit cell with geometrical dimensions (Designed parameters: u_w= 4.4 mm, u_h= 4 mm, u_p = 2 mm, t_a = 0.4 mm, t_b = 0.2 mm).

The unit cell has been studied under the periodic arrangement as shown in Fig. 4.25(a) using Ansys HFSS [166]. The patterns of the unit cell are based on different practical applications. Floquet port is used in the simulator to invoke the periodic boundary conditions with various Floquet modes. Fundamentally, Floquet modes are plane waves with propagation direction set by the frequency and geometry of the periodic structure. Floquet Ports are used exclusively with periodic structures defined by primary and secondary boundaries (Coupled Lattice Pair). They contain plane waves whose frequency, phasing, and the geometry of the periodic structure determine the propagation direction viz., planar phased arrays and frequency selective surfaces. The periodically arranged unit cell exhibits 0° reflection phase at 10 GHz and 17.65 GHz as observed from Fig. 4.25(b). The variation in the reflection phase is bounded between ±180° over the frequency region 1 GHz to 20 GHz as seen from Fig. 4.25(b).

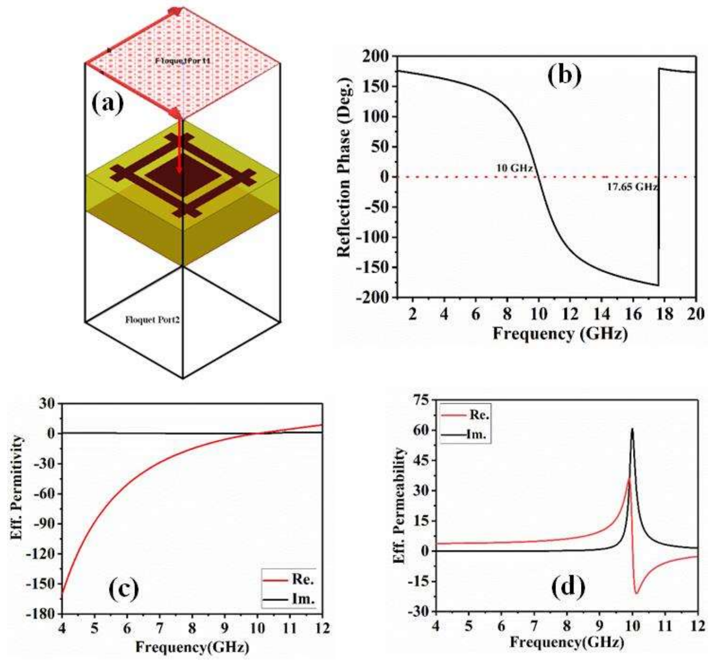

Fig. 4.25. (a) The three-dimensional view of the unit cell (b) reflection phase characteristics with respect to frequency (c) effective permittivity of the unit cell (d) effective permeability of the unit cell.

Further, the real and imaginary parts of the effective permittivity and the effective permeability have been extracted by the S-parameter retrieval method [47]-[49], and the retrieved parameters of the same have been shown in Fig. 4.25(c) and Fig. 4.25(d), respectively. It is observed that the MS layer behaves as an ENG material ($\varepsilon < 0$ and $\mu > 0$) below 10 GHz while the MNG behavior ($\varepsilon > 0$ and $\mu < 0$) has been observed above 10 GHz. Hence, 10 GHz is considered as the plasma frequency since the effective permittivity is zero at 10 GHz; thereby yielding a zero-index metamaterial. The zero-phase reflection bandwidth of the MS significantly influences the bandwidth of the array of unit elements. It has also been found that the increase in equivalent inductance is responsible for the enhancement of bandwidth in MS structures [171]–[173].

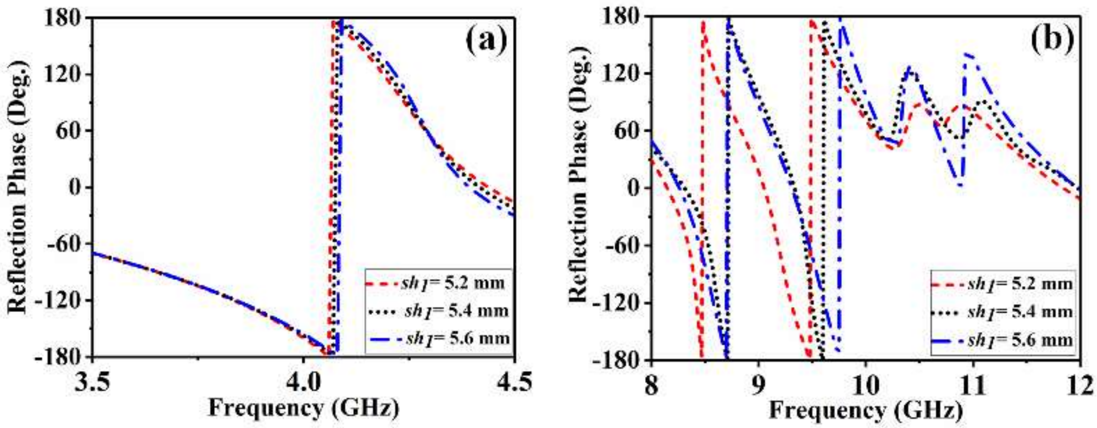

Fig. 4.26. Variation of the reflection phase of the MS at two different frequency bands (a) 4-4.5 GHz (b) 8-12 GHz.

The equivalent input impedance of an MS unit element can be expressed as the parallel combination of the impedances of the periodic pattern and the grounded dielectric layer impedance. This results in the equality between the MS reflection bandwidth and the bandwidth of a parallel LC circuit with net inductance and capacitance of L_m and C_m, respectively as seen from (4.6)

$$BW=\frac{\omega_0^2 L_m}{Z_0}=\frac{1}{C_m Z_0} \tag{4.6}$$

where $\omega_0 L_m$ represents the impedance, ω_0 which has a dimension of rad/sec represents the bandwidth, Z_0 is the free space impedance. This implies that by lowering C_m, the MS zero-phase bandwidth can also be enhanced which can be accomplished by forming a wide slot gap between the centered patch and the rectangular strips on each arm of the proposed MS unit cell illustrated in Fig. 4.24. The etched slot gap between the centered patch and the rectangular strips of the unit cell generates a capacitive effect and the series combination of these capacitances reduces the total equivalent capacitance of the MS structure; thereby improving the zero phase reflection bandwidth.

In this MS antenna design, a 7×7 array of periodic unit cells have been placed above the modified patch antenna in a superstrate configuration. Here, the superstrate and the ground layers have been separated by a height of sh_1 as illustrated in Fig. 4.17(a). The resonant conditions of this superstrate based MS antenna can be expressed in (4.7-4.8) [174]-[176]

$$\varphi_s + \varphi_g - \frac{4\pi h}{\lambda} = 2N\pi, \quad N = 0, \pm 1, \pm 2\ldots \tag{4.7}$$

$$f = \frac{c}{4\pi h}\left(\varphi_s + \varphi_g - 2N\pi\right) \tag{4.8}$$

where h is the spacing between the superstrate layer and the ground, φ_s and φ_g are the reflection phases of the superstrate layer and the metal ground plane respectively, and λ is the operating wavelength in the substrate, differing from the free space wavelength λ_0 in the conventional air-filled antenna. Since λ is shorter than λ_0, as observed from (4.7), the height h of the proposed MS antenna is smaller compared to the conventional air-filled one.

The reflection phase characteristics of the reflection coefficient for different heights (sh_1) between the superstrate layer and the ground have been studied in Figs. 4.26-4.27. It can be seen that the phases can be easily turned by altering sh_1, which in turn controls the resonant condition as evident from (4.8). Moreover, the parametric study of the gap between two consecutive unit cells along the horizontal direction (p) and vertical direction (p_1) are shown in Fig. 4.28(a) and Fig. 4.28(b). It has been observed that at p = 5.2 mm, p_1 = 5 mm, and sh_1 = 5.4 mm, the antenna exhibits good impedance matching with improved bandwidth.

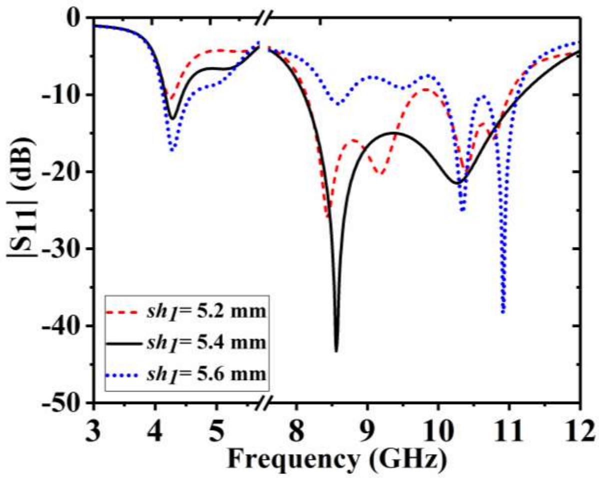

Fig. 4.27. The plot of $|S_{11}|$ (dB) with respect to the frequency at sh_1 variations of the MS antenna.

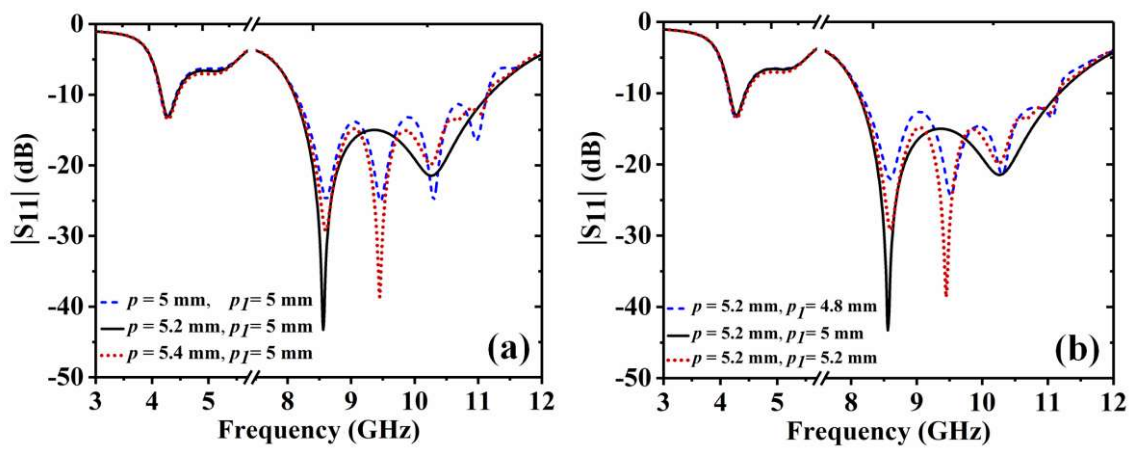

Fig. 4.28. Plot of $|S_{11}|$ (dB) with respect to frequency (a) at constant p_1 = 5 mm and p variations (b) at constant p = 5.2 mm and p_1 variations.

The equivalent circuit model of the antenna loaded with the MS superstrate has been subsequently developed as shown in Fig. 4.29(a). The air gap layer between the patch and the MS has been represented with the parameters R_a and C_a connected in parallel with the antenna circuit while R_m, C_m, and L_m are the equivalent lumped elements used for unit cells of the MS. Further, R_m represents the radiation resistance of the metasurface (MS) resonator.

L_m and C_m are the respective equivalent inductance and capacitance values of the MS slot resonator. R_m in the Foster canonical form representation for the MS takes care of both radiation and ohmic losses as mentioned earlier [168]-[170]. C_{cm1} and C_{cm2} are the equivalent coupling capacitances between the neighboring unit cells along with vertical and horizontal directions of the MS layer.

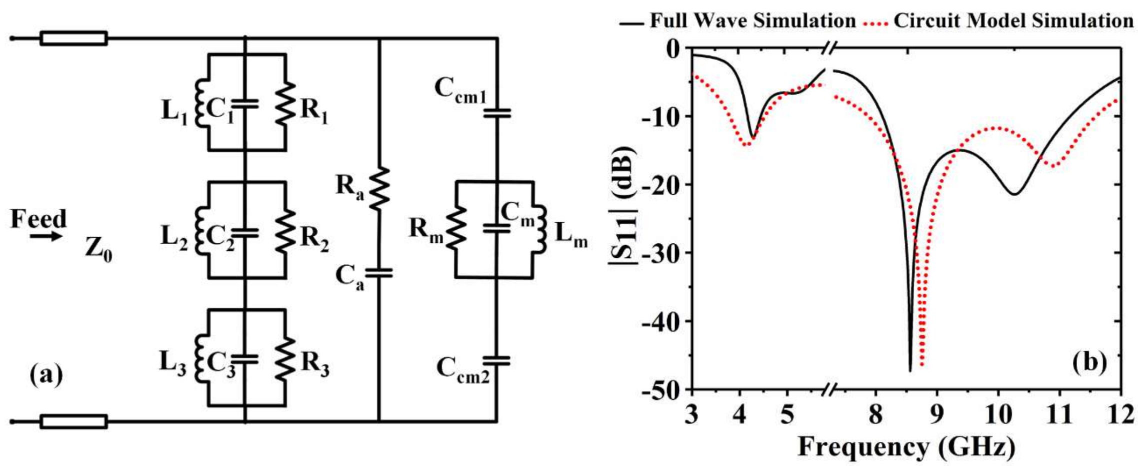

Fig. 4.29. (a) The equivalent electrical circuit model of the proposed patch antenna with the metasurface as a superstrate (b) Plot of $|S_{11}|$ (dB) with respect to frequency using Ansys HFSS simulation vs ADS simulation characteristics comparison.

The lumped circuit parameters in Fig. 4.29(a) have been calculated from Keysight ADS simulation analysis and these are: $R_a = 377\ \Omega$, $C_a = 220.65$ pF, $R_m = 94.5\ \Omega$, $C_m = 1.186$ pF, $L_m = 0.273$ nH, $C_{cm1} = 0.35$ pF, $C_{cm2} = 0.35$ pF and $Z_0 = 50\ \Omega$. The additional circuit component values for the MS as a superstrate have been derived by fixing the same circuit component values of the radiating patch as per Fig. 4.22. The comparison of the reflection coefficient responses of the numerical simulation and the circuit model simulation is shown in Fig. 4.29(b) which offers a good resemblance between the two. It can be seen that the antenna loaded with MS superstrate layer operates at dual frequency regions with the fractional bandwidths of 6.1% and 35.15% at 4.26 GHz and 8.62 GHz, respectively. This antenna design has been considered as the proposed antenna configuration due to the significantly improved characteristics.

4.5 Results and Analysis of the Multi-Layered Metasurface Antenna

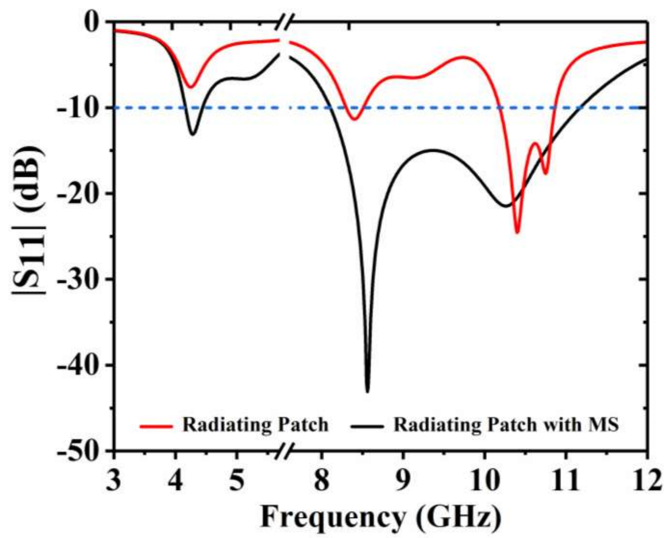

Fig. 4.30. The plot of $|S_{11}|$ (dB) with respect to frequency (GHz) of the proposed antenna.

The reflection coefficient characteristics of the proposed MS antenna along with the radiating patch antenna have been shown in Fig. 4.30. The radiating patch operates over two frequency regions ranging from 8.3 GHz to 8.51 GHz and 10.19 GHz to 10.87 GHz with fractional bandwidths of 2.4% and 6.5% respectively. This patch antenna exhibits the narrowband behaviour of impedance bandwidth with low return loss. The performance of this radiating patch has been significantly improved by incorporating a 7×7 order MS layer with air spacer in the superstrate configuration. The loading of the MS superstrate layer results in the dual-band response of the antenna operating from 4.18 GHz to 4.44 GHz and 8.11 GHz to 11.14

GHz with the respective fractional bandwidths of 6.1% and 35.15% at 4.26 GHz and 8.62 GHz as evident from Fig. 4.30. The maximum return loss of 42 dB has been achieved at 8.62 GHz.

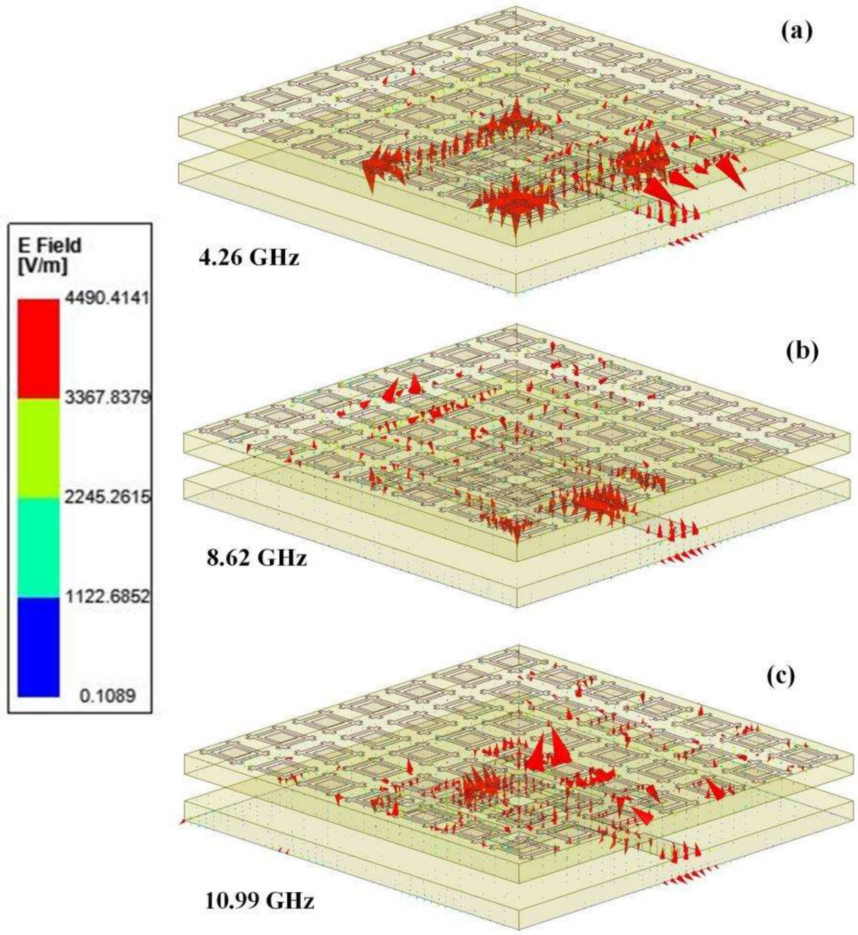

Fig. 4.31. Electric field distributions at (a) radiating patch (b) 7×7 order metasurface at different operating frequencies.

The electric field distributions in the radiating patch and the MS layer at 4.26 GHz, 8.62 GHz and 10.99 GHz have been studied as shown in Fig. 4.31. The field distribution of the radiating patch is found to be maximum along the edge of the annular slot regions and the strength of the fields is high around the unit cells of the MS layer. Moreover, the electric field is quite intense at the rectangular strips of the unit cells at these frequencies. Further, the surface current distributions in the radiating patch and the MS layer at 4.26 GHz, 8.62 GHz and 10.99 GHz have been demonstrated in Fig. 4.32(a) and Fig. 4.32(b) respectively. The surface currents are more intense at the slot in the patch and also in the aperture of metasurface unit cells as revealed from Fig. 4.32. It is further observed that the concentration of surface current at 10.99 GHz is more as compared to other operating frequencies due to maximum field distribution among unit cell slots on the top surface.

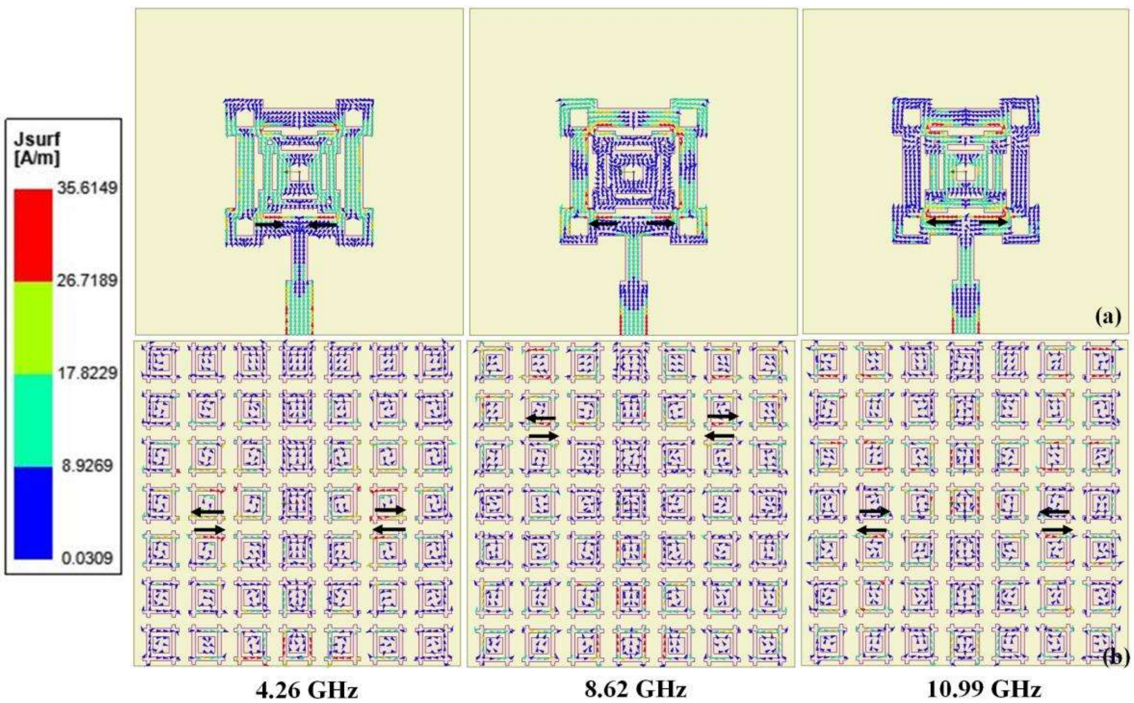

Fig. 4.32. Surface current distributions at (a) radiating patch (b) 7×7 order metasurface at different operating frequencies.

The proposed antenna has been printed on FR4 dielectric using LPKF PCB Prototyping Instrument [130]. The top view of the conventional patch with a 50 Ω SMA connector has been shown in Fig. 4.33(a). The pictorial representation of the fabricated 7×7 MS layer has been shown in Fig. 4.33(b). The overall dimensions of both the radiating patch and the MS are the same. The three-dimensional view of the proposed fabricated prototype has been illustrated in Fig. 4.33(c) in which two layers have been separated by foam as the electromagnetic properties of the air spacer and foam are nearly identical while foam offers mechanical support to the structure. The antenna prototype has been measured using the Keysight FieldFox Vector Network Analyzer (VNA) N9951A [154]. The return loss profile of the fabricated sample has been measured using VNA and presented in Fig. 4.33(d).

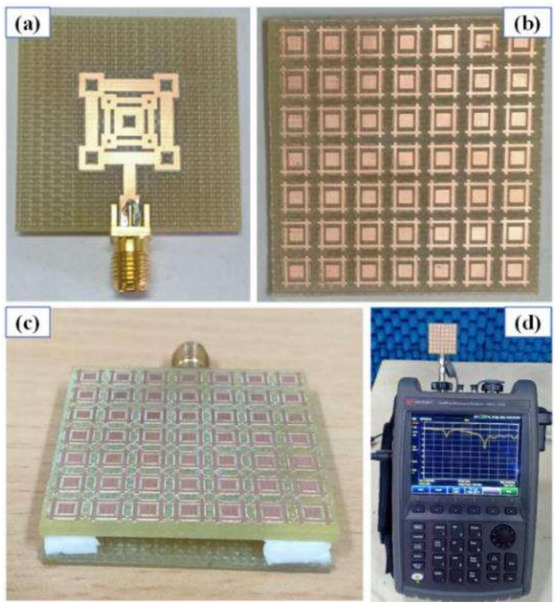

Fig. 4.33. Proposed fabricated prototype (a) Conventional patch (b) top view of 7×7 order metasurface (c) Three-dimensional view of the proposed antenna (d) S-parameter measurement using VNA.

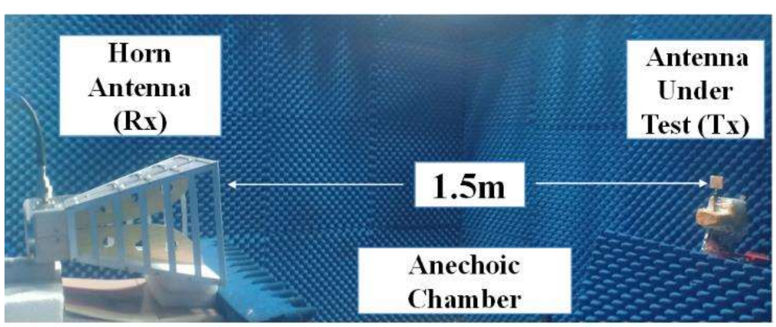

Fig. 4.34. Radiation pattern measurement of the proposed antenna using an anechoic chamber.

The far-field radiation characteristics of this antenna have been measured in the anechoic chamber and the experimental set-up has been shown in Fig. 4.34. In this measurement, the broadband horn antenna [155] has been considered as receiving antenna while the proposed fabricated antenna with MS as a superstrate has been used as the transmitting one.

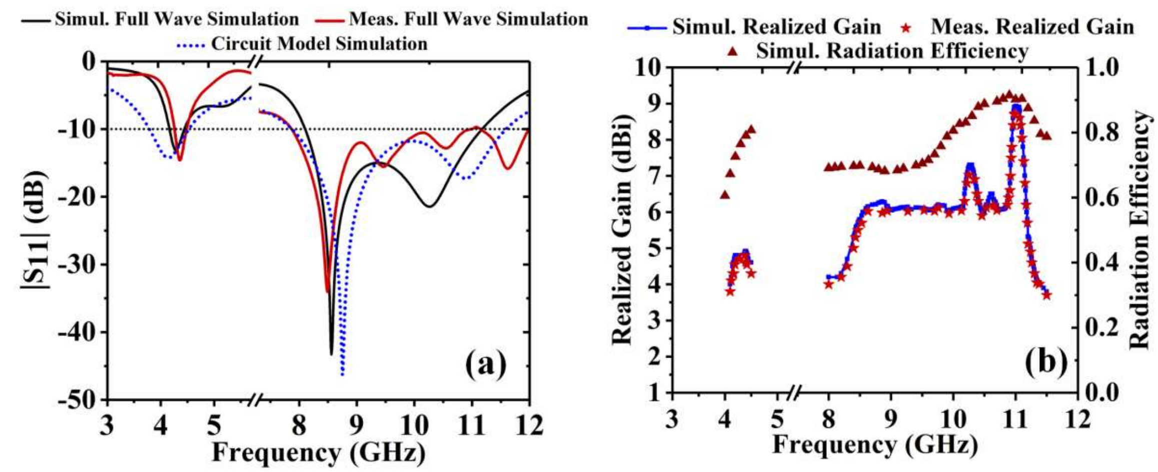

Fig. 4.35. (a) The plot of the simulated and measured $|S_{11}|$ (dB) along with circuit model simulation with respect to frequency (b) Responses of realized gain (dBi) and radiation efficiency with respect to frequency.

The comparison of the simulated and the measured reflection coefficient characteristics of the proposed prototype along with the reflection coefficient response achieved by the ADS circuit model have been illustrated in Fig. 4.35(a). The experimentally measured 10 dB impedance bandwidth has been realized in the frequency ranges 4.24 GHz-4.48 GHz and 7.87 GHz-11.01 GHz. Hence, the experimental reflection coefficient response has followed the simulated characteristics as well as the circuit model response. The far-field antenna gains and radiation efficiencies [74] of the proposed prototype with respect to frequencies have been shown in Fig. 4.35(b) where the measured gains have been compared with the simulated one. In the proposed prototype, the maximum simulated realized gain is 8.91 dBi whereas the experimentally measured realized gain of 8.72 dBi has been achieved. There is a variation in the radiation patterns across the operational bands that may be due to leakage of out of phase fields from few slots at patch, ground slots or the unit cells of the metasurface. The presence of coupling currents in the device may be due to less interspacing of the unit cells and the patch. However, such distortion at high frequency is still acceptable for wireless applications under multipath environment as the proposed antenna's cross-polarized levels remain lower than the co-polarized ones. Besides, it has been further observed that the maximum radiation efficiency of the proposed antenna is 91% at 10.99 GHz. The radiation efficiency improvement is due to the combined effect of the slotted patch and the 7×7 order metasurface. The planar MS structure is usually a high impedance surface that can modulate the electromagnetic fields excited by a patch resonator. The antenna efficiency value is influenced by a number of factors, including antenna geometry, beam pattern, and frequency reuse strategy. In some cases, the highest antenna efficiency does not lead to more effectiveness in some practical applications; hence, an intermediate efficiency value is preferable. Here the efficiency value is increased to 91% as it includes the conductor loss, dielectric loss, and ohmic loss. The actual radiation efficiency will be lower in practise. The slight difference between simulated and measured results in Fig. 4.35 is attributed due to the fabrication tolerances like the copper loss of the FR4 dielectric at the time of polishing and soldering between the dielectric substrate and SMA connector.

The simulated and measured radiation patterns of the proposed antenna along E-plane ($\varphi = 0^0$) and H-plane ($\varphi = 90^0$) at 4.26 GHz, 8.62 GHz, and 10.99 GHz have been illustrated in Fig. 4.36(a) and Fig. 4.36(b) respectively. The MS antenna radiates along the boresight direction both in E- and H-planes at all the operating frequencies; however, along H-plane at

8.62 GHz the antenna pattern deviates toward $\pm 30^0$. It is also evident from Fig. 4.36 that the measured cross-polarized levels of the proposed antenna remain below 10 dB than that of the co-polarized ones in the E-plane while in the H-plane, the cross-polarized levels remain below 25 dB from the co-polarized levels at all the operating frequencies. Hence, the antenna's radiation patterns are stable at the operating frequencies centered at 4.26 GHz, 8.62 GHz, and 10.99 GHz. The radiation characteristics at the mentioned frequencies have also been validated experimentally while there is a little discrepancy between the simulated and measured results which may be due to the fabrication tolerances, dielectric loss, adaptor, and cable losses incurred during the far-field measurement.

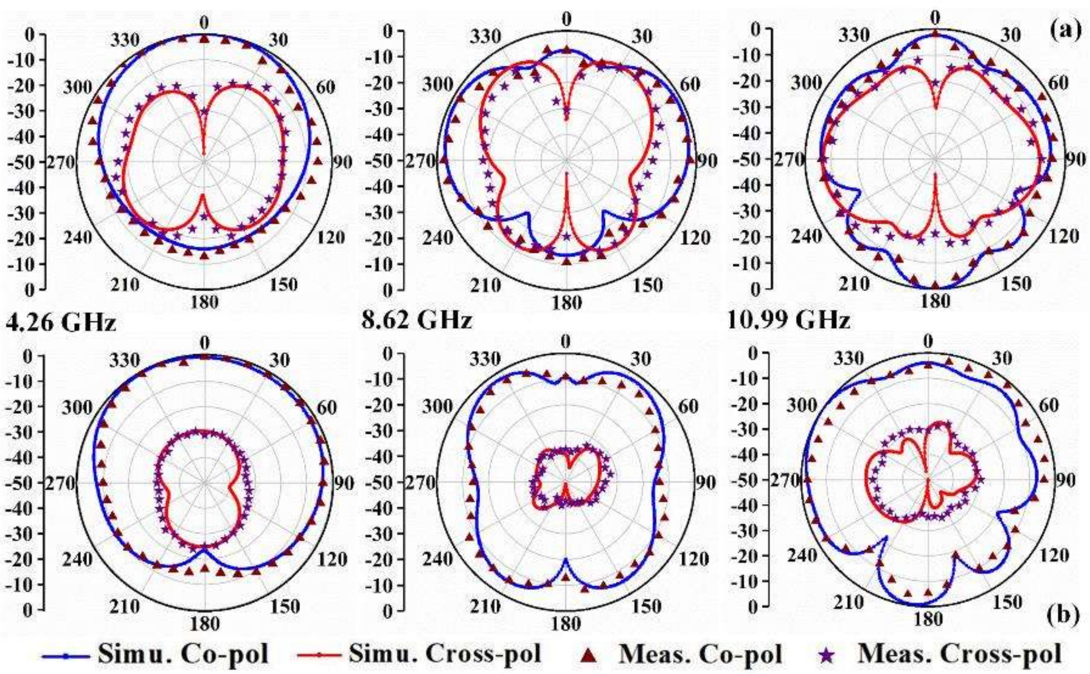

Fig. 4.36. Radiation pattern (a) E-plane co-polarized and cross-polarized and (b) H-plane co-polarized and cross-polarized at different operating frequencies within the proposed structure.

Table 4.4 Comparative Study of Proposed Metasurface Antenna with some Reported Metasurface Antennas

Antenna Literature	Overall Dimensions	Operating Frequency (GHz)	Antenna Design Complexity	Fractional BW (%)	Gain (dBi)	Efficiency (%)	Antenna Type
Gao *et al.* [2]	$\pi\times0.22\lambda_0\times0.22\lambda_0\times0.03\lambda_0$	2.45, 5.5	High	4.9, 15.7	7.7	-	Metasurface Antenna for Body-Centric Communications
Pan *et al.* [141]	$1.3\lambda_0\times1.3\lambda_0\times0.6\lambda_0$	5	High	28.4	8.2	39	Superstrate technology with MS
Kim *et al.* [143]	$1.2\lambda_0\times1.2\lambda_0\times0.4\lambda_0$	5.75	Very High	2.7	6.8	_	Holey dielectric superstrate structure
Zheng *et al.* [150]	$2.8\lambda_0\times2.8\lambda_0\times0.1\lambda_0$	10.5	Very High	18.5	8.1	_	AMC
Alibakhshikenari *et al.* [156]	$2.4\lambda_0\times3.2\lambda_0\times0.04\lambda_0$	8	Low	14.5	7	88.7	Antenna arrays based on metamaterial EBG structure
Zhang *et al.* [177]	$0.69\lambda_0\times0.69\lambda_0\times0.04\lambda_0$	2.45, 3.71	Low	4.1, 24.2	2.1	91	Radial CRLH-TL-based antenna
Yang *et al.* [178]	$0.56\lambda_0\times0.56\lambda_0\times0.01\lambda_0$	2.38, 3.5	High	4.1, 7	7.7	63.3	Wearable Textile Antenna
Mattsson *et al.* [179]	$1.2\lambda_0\times1.2\lambda_0\times0.0066\lambda_0$	2.45, 5.5	High	36, 8	7.52	45	Rectenna based on microstrip patch
Liu *et al.* [180]	$1.3\lambda_0\times0.9\lambda_0\times0.14\lambda_0$	2.6, 3.5	High	7.7, 5.7	8.6	88	Metasurface based two closely packed antenna
Samantaray *et al.* [181]	$0.9\lambda_0\times0.9\lambda_0\times0.29\lambda_0$	10.44	Low	7.66	7.57	_	Slotted patch with superstrate structure
Ke *et al.* [182]	$1.1\lambda_0\times0.94\lambda_0$, Profile $t>0.03\lambda_0$	9.25	High	16.2	8.5	_	DRA type metamaterial antenna
Sharma *et al.* [183]	$3.6\lambda_0\times3.6\lambda_0\times0.14\lambda_0$	13.6	High	9	9.1	_	Chess board-based polarization conversion MS
Youse *et al.* [184]	$1.7\lambda_0\times1.7\lambda_0\times0.41\lambda_0$	14.12, 15.37	High	1.7, 1.3	10	_	Fabry-Pérot cavity antenna
Chen *et al.* [185]	$2.04\lambda_0\times2.04\lambda_0\times0.55\lambda_0$	7.28, 8	Very High	1.1, 2.5	13.25	_	Metamaterial-Inspired antenna
Ahmed *et al.* [186]	$1.8\lambda_0\times1.2\lambda_0\times0.01\lambda_0$	1.8, 2.6	High	_	10.2	85.17	EBG-Based Periodically Modulated Metasurface
Gu *et al.* [187]	$2.22\lambda_0\times0.75\lambda_0\times0.05\lambda_0$	3.5, 4.9	High	8.5, 4.08	12.43	_	Metasurface Antenna Based on Common Feeding Network
Proposed Design	$1.03\lambda_0\times1.03\lambda_0\times0.15\lambda_0$	4.26, 8.62	Low	6.1, 35.15	8.72	91	Modified slotted patch with MS

The performance comparison of the proposed metasurface antenna with some other recently reported high-performance antennas have been shown in Table 4.4. It is seen from Table 4.4 that the proposed low-profile antenna exhibits significantly enhanced gain along with improved bandwidth and more compactness. The reported antennas in [2], [177], [178], [181] are low profile in nature; however, these antennas operate over a narrower bandwidth and lower gain. Some of the reported antennas in [183]-[187] have achieved superior gain but those were designed in larger dimensions on a substrate with high relative permittivity. In the proposed dual-band antenna prototype, the design complexity is low as compared to the previously reported ones. In addition, the efficiency of this prototype has been enhanced to 91% due to the improved realized gain of 8.72 dBi. Thus, the proposed antenna can be used for various C- and X-band applications as the antenna performances are significantly enhanced.

4.6. Concluding Remarks

The first MS antenna presents a new design of a metasurface-based corner cut rectangular patch antenna in which the radiating patch and the MS have been designed in the same substrate. The proposed metasurface antenna operates over dual frequencies with impedance bandwidths (S_{11} < -10dB) of 4.02% and 28.24% at 9.20 GHz and 11.65 GHz respectively. The antenna design is simple and compact with dimensions of $1.16\lambda_0 \times 1.82\lambda_0 \times 0.06\lambda_0$, where λ_0 is the free-space wavelength at 11.65 GHz. It has an optimum gain that is in excess of 10.6 dBi and radiates with a maximum radiation efficiency of 67% at 14.44 GHz. The introduction of SRR to the patch and non-uniform arrangement of metasurface has been found to be very useful towards the increase of the gain. The prototype exhibits high gain with unidirectional radiation at the desired frequencies. The measured results of the antenna prototype are in good agreement with the simulated ones.

In the second antenna design, the limitation of the radiation efficiency has been improved by using a multi-layered arrangement. This antenna offers directional radiation characteristics with dual-band impedance bandwidth for C- and X-bands applications. The proposed prototype consists of a slotted modified patch and a 7×7 array of periodic metasurface (MS) arranged in a superstrate configuration. The antenna operates at two different frequency regions in which the fractional bandwidths of 6.1% and 35.15% have been achieved at 4.26 GHz and 8.62 GHz, respectively. The antenna radiates along the boresight direction with a maximum realized gain of 8.91 dBi and has a maximum radiation efficiency of 91% at 10.99 GHz. The equivalent circuit model with the component values of the modified slotted patch antenna and the same patch with MS as a superstrate have been subsequently developed in the manuscript. Experimentally measured impedance response of the fabricated prototype offers good matching with the simulated and the circuit model responses of the antenna; thereby validating the design. The measured far-field characteristics of the antenna are also in good resemblance with the simulated ones. This antenna works in the X-band region. X band antennas are used for radar applications in civil, military, and different organizations for weather monitoring, air traffic control, maritime vessel traffic control, defense tracking, and vehicle speed detection for law enforcement.